Institute of Physics
Master Engineering Physics

Master's thesis:

Wind speed measurements in an offshore wind farm by remote sensing. A comparison of radar satellite TerraSAR-X and ground-based LiDAR systems

Author: Julian Hieronimus

First Examiner: Prof.Dr. Martin Kühn[1]
Second Examiner: Dr.rer.nat. Susanne Lehner[2]

Supervisors: Jörge Schneemann[1]
Dr. Sven Jacobsen[2]
Juan-José Trujillo[1]

Oldenburg, 29th of June 2015

Reviewed version 27th of November 2015

[1]ForWind - Carl von Ossietzky Universität Oldenburg
[2]German Aerospace Center (DLR), Remote Sensing Technology Institute, Bremen, Germany

Abstract

In offshore wind industry there is a high demand for precise wind turbine wake models, which allow a prediction of the wind farm's power output. For validation and improvement of these models, highly resolved wind field measurements of the wind flow in- and around offshore wind farms are needed. This can be provided by the measurement systems Doppler-LiDAR and SAR-Satellite. Doppler-LiDAR directly measures the local windfield by changing the direction of the LiDAR's laser beam and has found a wider application in offshore related research. SAR-Satellite indirectly measures a snapshot of the windfield via the ocean's surface roughness and has been validated against measurement buoys, but not compared to other highly resolved wind fields up to now. In this Master Thesis the agreement of highly resolved wind fields by Doppler-LiDAR and SAR-Satellite is investigated for free stream and wake conditions. To allow a comparison of the differently distributed measurement data from LiDAR and SAR, processing methods are developed and presented in this Thesis. In free stream conditions a good correlation between the measured LiDAR and SAR wind field structures is observed, indicating that SAR is a promising technology for retrieval of wind field measurements in free stream. In wake conditions no agreement can be confirmed due to larger time lags between LiDAR and SAR measurements.

In der Offshore-Windindustrie gibt es einen großen Bedarf an präzisen Nachlaufmodellen zur Vorhersage der Leistungsabgabe eines Offshore-Windparks. Zur Validierung und Verbesserung dieser Modelle werden hochaufgelöste Windfelder in- und außerhalb des Windparks benötigt. Diese können unter anderem von den Messystemen Doppler-LiDAR und SAR-Satellit bereitgestellt werden. Doppler-LiDAR vermessen das lokale Windfeld direkt durch Ausrichten des Laserstrahls und haben bereits eine weite Verbreitung in der Offshore Windenergieforschung erlangt. SAR-Satellit Windfelder werden indirekt über die Rauhigkeit der Meeresoberfläche ermittelt und wurden bereits gegen Messbojen, aber bislang noch nicht gegen andere hochaufgelösten Windfelder validiert. In dieser Masterarbeit wird die Übereinstimmung von hochaufgelösten Windfeldern mit Doppler-LiDAR und SAR-Satellit für freie Strömung und im Nachlauf von Windenergieanlagen untersucht. Methoden zur Prozessierung der räumlich unterschiedlich verteilten Messdaten von LiDAR und SAR werden in dieser Arbeit entwickelt und präsentiert. In freier Strömung wurde eine gute Korrelation zwischen den mit LiDAR- und SAR gemessenen Windfeldstrukturen beobachtet, was aufzeigt, dass SAR eine vielversprechende Technologie für hochaufgelöste Windfeldmessungen in freier Strömung darstellt. Vergleiche der Windfelder im Nachlauf zeigen keine gute Übereinstimmung, was in dem großen Messzeitunterschied des verwendeten Szenarios für die LiDAR und SAR Messung begründet liegt.

Copyright notice

Oldenburg, the 29th of June 2015

Julian Hieronimus

Delcaration of own work

Herewith I assure that i wrote this thesis independently and have not used any sources other than those indicated in the references. Furthermore, I assure that I followed the general principles of scientific work and publications, as laid down in the guidelines of good scientific practices by the Carl von Ossietzky Universität Oldenburg.

Hiermit versichere ich, dass ich diese Arbeit selbstständig verfasst und keine anderen als die angegebenen Quellen und Hilfsmittel benutzt habe. Auerdem versichere ich, dass ich die allgemeinen Prinzipien wissenschaftlicher Arbeit und Veröffentlichung, wie sie in den Leitlinien guter wissenschaftlicher Praxis der Carl von Ossietzky Universität Oldenburg festgelegt sind, befolgt habe.

Oldenburg, the 29th of June 2015

Julian Hieronimus

Acknowledgement

I would like to express my gratitude to my direct supervisor Jörge Schneemann for the very good and dedicated guidance, support and always helpful comments throughout the course of this master's thesis.

Special thanks to Sven Jacobsen for his technical support and always willingness to help to answer any question about wind field measurements with TerraSAR-X.

Many thanks to Martin Kühn and Susanne Lehner for the supervision of this master's thesis and for offering this beautiful topic. At this point i would also like to express my gratitude for giving me the possibility to present the results of my thesis at the ISRSE36 conference in Berlin.

My thanks to all the members of the Wind Energy Systems working group at ForWind in particular Wilm Friedrichs, Juan-José Trujillo, Davide Trabucchi and Hauke Beck for the very helpful comments and discussions.

I would like to take this opportunity to thank my colleagues and friends Janna Seifert, Marijn van Dooren, Augusto Bustamante and Christian Hempen for the always willingness to help, the nice working atmosphere and for a couple of pleasant evenings aside the university. Special thanks to Janna Seifert for the dedicated help to give my thesis a final polish.

I cannot thank enough nor have any words at all to express my gratitude for the long standing support of my parents and family in all situations, which always motivated me to give my very best.

The lidar measurements were performed in the frame of the research project GW Wakes, funded by the German Federal Ministry for Economic Affairs and Energy (BMWi) based on a decision of the Parliament of the Federal Republic of Germany (grant number 0325397A).

I thank Deutscher Wetterdienst (DWD) for providing the COSMO-DE analysis data.

Contents

List of Figures

List of Tables

Nomenclature

Quantity	Symbol	Unit
Section 2.1		
Horizontal wind velocity	V	[m/s]
Line of sight wind velocity	V_{Los}	[m/s]
Relative angle between V_{Los} and V	δ	[deg]
Doppler frequency shift	f	[Hz]
Frequency of emitted wave	f_0	[Hz]
Speed of light	c	[m/s]
Carrier to Noise Ratio	CNR	[dB]
Azimuth angle of LiDAR unit	Φ	[deg]
Elevation angle of LiDAR unit	χ	[deg]
Elevation of wind flow	χ_{wind}	[deg]
Relative angle between Φ and wind direction	α	[deg]
Relative angle between χ and χ_{wind}	δ	[deg]
Horizontal wind speed components	u, v	[m/s]
Vertical wind speed component	w	[m/s]
Section 2.2		
Wavelength of radio pulse	λ_r	[m]
Normalized Radar Cross-Section (NRCS)	σ_0	[-]
Radar incidence angle	Θ	[deg]
Radar range resolution	r_a	[m]
Radar pulse width	τ	[m]
Radar pulse bandwidth	β	[m]
Satellite antenna length	d_a	[m]
Azimuth resolution	ϑ_a	[deg]
Synthetic aperture length	L_a	[m]
Section 2.3		
Frictional velocity	u_*	[m/s]
Surface roughness length	z_0	[m]
Stability parameter	Ψ	[m/s]
Obhukov length	L	[m]
Air temperature in 2 m height	T_{2m}	[K]
Soil temperature	T_S	[K]
Charnock coefficient	a_c	[-]
Wave age	c_{wave}	[-]
Phase speed	c_{ph}	[m/s]

Quantity	Symbol	Unit
Section 3.2		
Selection radius	R	[m]
Grid center distance	d	[m]
10 m wind speed	U_{10}	[m/s]
Empirically found XMOD2 coefficients	B_0, B_1, B_2	[-]
Relative viewing angle	ψ	[deg]
Section 3.3		
Accumulation time	t_{ac}	[s]
LiDAR pulse repetition frequency	f_p	[Hz]
LiDAR pulse duration	t_p	[ns]
Amount of samples per range gate	N_{fft}	[-]
Gaussian function	G(x)	[m/s]
Wake centre	l	[m]
Ambient wind speed	C	[m/s]
Maximal velocity deficit	A	[m/s]
Section 3.4		
Wind velocity error	σ_V	[m/s]
LiDAR line of sight accuracy	ΔV_{Los}	[m/s]
LiDAR azimuth accuracy	$\Delta\Phi$	[deg]
COSMO-DE wind direction accuracy	$\Delta\vartheta$	[deg]
Section 4.1.2		
Time lag between TS-X and LiDAR	Δt	[s]

1 Introduction

As part of the ongoing expansion of energy generation from renewable sources, offshore wind energy has received a large growth in many countries in the recent years. By end of 2014 offshore wind turbines with a cumulative capacity of 8000 MW were installed in Europe and are still increasing in number with a predicted growth of over 1000 MW of new offshore wind capacity installed every year (Corbetta et al., 2015). Wind speed measurements play a crucial role for the future development of offshore wind energy. Operators of offshore wind farms need reliable wind data for e.g. resource assessment as well as load and power estimations in order to ensure an economic operation of the wind farm. In wind energy related research a hot topic is the measurement and modelling of wind turbine wakes, which can cause power losses (Barthelmie et al., 2010) and increased loads of wind turbines (Lee et al., 2012). For wake studies detailed wind field information with a high spatial and temporal coverage and resolution is needed.
The most common methods to measure wind speeds offshore is the use of cup anemometers mounted on buoys (Queffeulou, 1991) or meterological masts (Neumann et al., 2004). While cup anemometers are able to measure high resolved time series they lack the spatial coverage needed to investigate wake development. Spaceborne scatterometers allow to obtain a snapshot of the wind field in 10 m height with a wide spatial coverage but low spatial resolution and low wind speed accuracy (Satheesan et al., 2015). Meso-scale weather models are able to simulate wind fields with a high spatial coverage from available wind data (Baldauf et al., 2009) but a low spatial and temporal resolution.
In recent years the remote sensing method Doppler-LiDAR (**Li**ght **D**etection **A**nd **R**anging) has found a wider application for scientific and commercial offshore wind measurements. LiDAR systems emit a laser beam to the atmosphere to measure radial wind velocities by detecting the Doppler shift of light backscattered from aerosols. LiDAR wind profilers scan a conical pattern with their laser beam to obtain the vertical wind profile above the device. LiDAR profilers have been applied on offshore met masts (Cañadillas et al., 2011), oil and gas platforms (Kindler and Oldroyd, 2010) and buoys (Gottschall et al., 2014).

Currently offshore wind related research has started to use scanning long range Doppler-LiDAR, able to measure the areal wind field by horizontally scanning with the LiDAR's laser beam (Schneemann et al., 2015). Scanning Doppler LiDAR is able to map horizontal areas with high spatial and temporal resolution (Butler et al., 2013). LiDAR systems are typically validated against meterological masts (Schneemann et al., 2014). LiDAR was applied to resolve wake structures behind wind turbines onshore (Aitken et al., 2014; Käsler et al., 2010) and offshore (Beck et al., 2015; van Dooren, 2014; Vollmer et al., 2015).
Spaceborne SAR (**S**ynthetic **A**perture **R**adar) satellites offer the possibility to retrieve a snapshot of the wind field offshore both with high spatial coverage and resolution. Wind speeds are obtained by observation of the radar backscatter from the ocean surface. The backscatter intensity depends on the roughness of the sea surface on a centimetre scale, which is driven by the wind flow. A geophysical model function (GMF) relates the radar backscatter to the 10 m wind speed. Different algorithms for the retrieval of the 10 m wind

speed have been developed and validated against point measurements by buoys (Li and Lehner, 2014) and coarse weather simulations (Hersbach, 2008). Comparisons between an airborne LiDAR wind profiler and SAR satellite have been carried out by (Werner et al., 1997, 2004). Spaceborne SAR has been applied for the estimation of wind farm wakes offshore (Hasager et al., 2015; Li and Lehner, 2013). However, the structures in wind fields obtained from SAR satellites have not been validated against data from other measurement systems with a high spatial resolution.
The availability of high resolved scanning LiDAR data enables for the first time the opportunity to compare SAR and LiDAR wind fields in detail. Considering the differences in the measurement principles, a match of small scale wind field structures is not self-evident.

On this basis, the major aim of this master's thesis is to investigate on the agreement of small scale wind field structures derived from SAR satellite and LiDAR in free stream and wake conditions. Concurrent measurements with scanning LiDAR and the satellite TerraSAR-X in and around the offshore wind farm *alpha ventus* located in the German North Sea are analysed. A processing method allowing for a comparison of the different spatial and temporal distributions of LiDAR and SAR data is developed.

After this introduction, chapter two highlights the fundamental measurement principles of LiDAR and SAR satellite. This is followed by a short overview of the vertical wind profile of the marine boundary layer (MABL) and wind turbine wake development. In chapter three a description of the experimental layout and available dataset is given. Furthermore the methods used to carry out a wind field comparison are presented. Results of the comparison in free stream and wake conditions are presented and discussed in chapter four. Finally a summary and conclusion is given in chapter five followed by an outlook on future research possibilities.

2 Theory

2.1 Fundamentals of pulsed-Doppler LiDAR measurements

In this introductory chapter, the basic principles of measurements with LiDAR systems will be highlighted and explained. A LiDAR system utilizes light signals to estimate specific parameters of the atmosphere such as composition or wind speed. By readjusting the azimuth-and elevation angles LiDAR devices are able to change the observation direction, and thus enabling measurements at arbitrary points in space within a given radius around the device. At this point it should be mentioned that within the scope of this thesis only pulsed-Doppler LiDAR systems are discussed. A detailed overview of the large number of different measurement principles and types of LiDAR systems is given by (Weitkamp et al., 2005).

2.1.1 Wind velocity estimation with Doppler LiDAR

In order to estimate the wind velocity, Doppler LiDAR systems make use of the Doppler effect from light scattering particles in the air flow. In Figure 1 the measurement principle of pulsed-Doppler LiDAR systems is shown schematically.

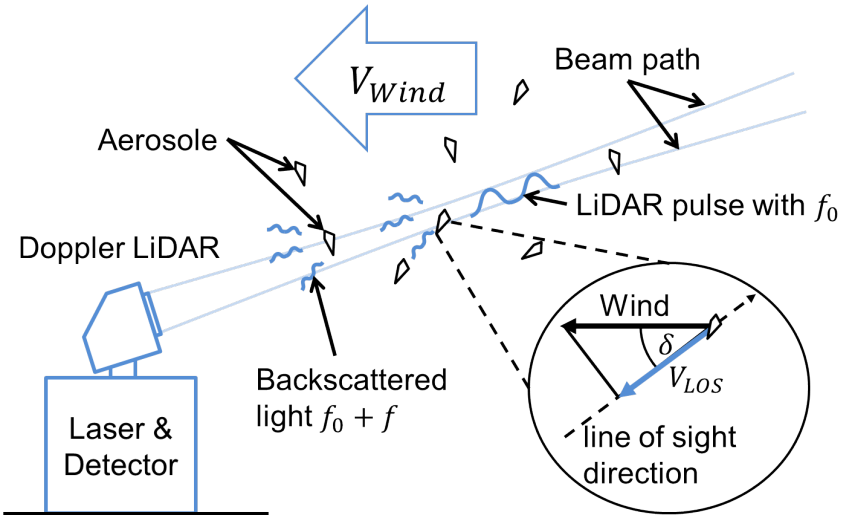

Figure 1: *Measurement principle of pulsed Doppler LiDAR system; The encircled enlargement shows the geometric dependency between the retrievable line of sight velocity V_{Los} and real wind velocity V under the measurement angle δ. Illustration based on (Trabucchi, 2013).*

The Doppler effect describes the frequency shift of a detected signal from a moving emitter with respect to the detected signal frequency of the same emitter at rest. The value of the frequency-shift can be estimated by the formula,

$$f = f_0 \cdot (1 + V/c) \tag{1}$$

where V denotes the motion speed of the emitter and f represents the Doppler frequency shift in respect to the emitter frequency f_0 at rest. If the frequency shift f and the original

frequency f_0 is known, the speed V of the moving particle can then be calculated using Equation 1.

For an effective detection via the Doppler effect, light emitting objects have to be existent in the atmosphere, which move with the same speed and direction as the wind flow. Especially the air-layers near to the ground are loaded with lightweight particles, which can easily be carried by the wind. Utilizing laser beams, the air particles are excited to a measurable light emission. This reflected emissions do show a Doppler frequency shift, which is detected by the LiDAR and used for the estimation of the wind speed. It is worth to mention that Doppler LiDAR devices are not able to measure the true wind speed directly, but the radial wind speed component V_{Los} in line of sight direction of the laser beam. Moreover a measurement of V_{Los} orthogonally to the wind movement is not possible, as in this case no relative movement takes place in line of sight direction of the laser beam (Werner, 2005).

2.1.2 LiDAR signal processing

Pulsed-Doppler LiDAR systems make use of the flight time of the laser pulse to determine the distance of a radial wind speed measurement V_{Los}. In combination with the known azimuth-and elevation angle of the emitted laser pulse, the position of the measurement in space can be located. Along its way through the atmosphere the laser pulse interacts with several particles, which absorb and reflect the irradiation of the laser pulse (see Figure 1). Hence, back scattered signals from different distances arrive successively at the detector, which result in a time dependant detection signal for each pulse as shown in Figure 2.

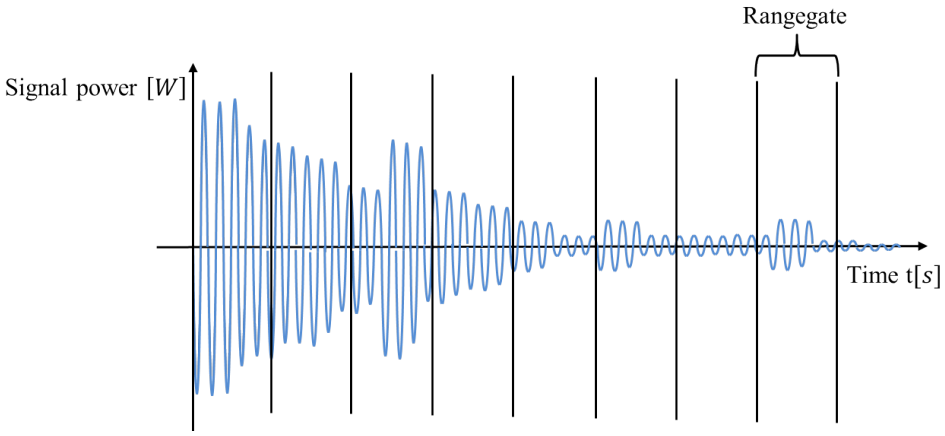

Figure 2: *Detection signal of one laser pulse measured by pulsed Doppler LiDAR. Illustration based on (Cariou and Boquet, 2010)*

In order to distinguish the Doppler frequency of the detected signal from frequencies caused by natural ambient light, the frequency spectrum of the detected signal has to be derived by a Fourier transformation. Since a Fourier transformation of the whole time series will lead to a loss of information about the distance of the measured radial wind speeds the detection signal is subdivided in several sections. These sections are called range gates, within each the frequency spectrum and the Doppler Peak is evaluated.

For a secure identification of the backscattered light signals, the power of the received signal P_{Signal} has to be greater than the background-noise P_{Noise}. This ratio is called CNR (**C**arrier to **N**oise **R**atio) and is defined in Equation 2.

$$CNR = 20 \cdot log(\frac{P_{Signal}}{P_{Noise}}) \tag{2}$$

The CNR is used as a first sign of quality for the estimated wind speed value. Especially backscattered signals from a greater distance do show a relatively weak CNR. Via averaging over several emitted LiDAR pulses the CNR value improves significantly, since the random frequencies in the background noise cancel each other (Cariou and Boquet, 2010).

Together with the pulse length of the laser pulse, the range gates determine the minimum spatial resolution in line of sight of the laser beam. In general, range gates can be selected arbitrarily narrow, whereupon the pulse length of the laser beam limits the minimal possible spatial resolution and in consequence a range gate with a width smaller than the pulse duration (full width at half maximum) will not lead to a finer spatial resolution. A further important factor is represented by the amount of samples used per range-gate for the estimation of the frequency spectrum. The less the amount of sample points, the faster the Fourier spectrum can be computed, but will also lead to a more rough resolution of the frequency spectrum and hence to increased uncertainties for the retrieval of the wind speed.

2.1.3 Estimation of wind-vectors

In order to calculate the real wind speed V from the line of sight measurements V_{Los} a transformation of V_{Los} on V has to be carried out given by the following relation in Equation 3,

$$V = \frac{V_{Los}}{cos(\alpha) \cdot cos(\delta)} \tag{3}$$

where α denotes the relative angle between the azimuth angle Φ of the LiDAR and the real wind speed direction ϑ in the x-y plane. The parameter δ represents the relative angle between the elevation angle χ of the LiDAR and the elevation angle χ_{wind} of the real wind speed. The transformation of the LiDAR V_{Los} values on the real wind speed V is illustrated in Figure 3.

Beside the known LiDAR azimuth and elevation angles Φ and χ, information about the wind direction angles ϑ and χ_{wind} is required in order to calculate the wind speed V in a point P. Using a single LiDAR system this information can be obtained by additional meteorological information from wind vanes, sonic anemometers or weather simulations or by sine fitting the LiDAR V_{Los} values. Another possibility is the usage of multiple LiDAR (multi LiDAR) systems measuring in point P. In order to fully calculate the horizontal u and v as well as the vertical wind component w in one point in space with multi LiDAR, a minimum of three different linear independent values for V_{Los} in this point are required.

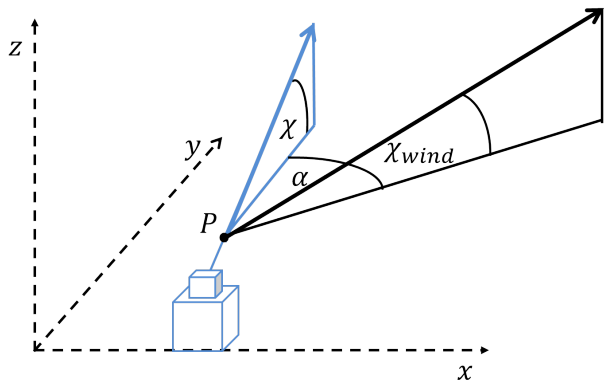

Figure 3: *Transformation of line of sight wind speed (blue line) on real wind speed (black line) in point P with one LiDAR. In point P the same coordinate system spanned by the vectors x, y and z is used as a reference for the angles.*

The radial wind vectors V_{Los} of the LiDAR systems can be derived by trigonometrical relations of the wind components, which are shown schematically for two LiDAR devices in Figure 4. The shown LiDAR units are placed on the same plane with a horizontal distance and measure the wind speed horizontally with changing azimuth and fixed elevation angle (PPI-Scan). The azimuth angles Φ_1 and Φ_2 are specified from the north direction as shown in the Figure 4. Given the V_{LOS1} and V_{LOS2} vectors with their specific azimuth angles Φ_1 and Φ_2 the wind components u and v can be derived by geometric relations. The V_{Los} is then the sum of the single wind components u and v shown in Equation 4 and 5 below.

$$V_{LOS1} = u \cdot sin(\Phi_1) + v \cdot cos(\Phi_1) \tag{4}$$

$$V_{LOS2} = u \cdot sin(\Phi_2) + v \cdot cos(\Phi_2) \tag{5}$$

The real wind speed can then be retrieved by the magnitude of the calculated components u and v. If more than two LiDAR system are used, the general formulation shown in Equation 6 can be used for estimation of the 3D wind components u, v and z (Stawiarski et al., 2013). It has to be mentioned that the sine and cosine terms in Equation 6 can be swapped depending on the reference axis selected for the elevation-and azimuth angles. In the shown case the elevation angles are specified from the perpendicular bisector, while the azimuth angles are specified from the y-axis.

$$\begin{pmatrix} V_{LOS1} \\ V_{LOS2} \\ V_{LOS3} \end{pmatrix} = \begin{bmatrix} sin(el_1) \cdot sin(\Phi_1) & sin(el_1) \cdot cos(\Phi_1) & cos(\Phi_1) \\ sin(el_2) \cdot sin(\Phi_2) & sin(el_2) \cdot cos(\Phi_2) & cos(\Phi_2) \\ sin(el_3) \cdot sin(\Phi_3) & sin(el_3) \cdot cos(\Phi_3) & cos(\Phi_3) \end{bmatrix} \cdot \begin{pmatrix} u \\ v \\ w \end{pmatrix} \tag{6}$$

Based on Equation 6 the Equations 4 and 5 can be derived by inserting for the elevation angles el_1 and el_2 a value of 90° and neglecting V_{LOS3}.

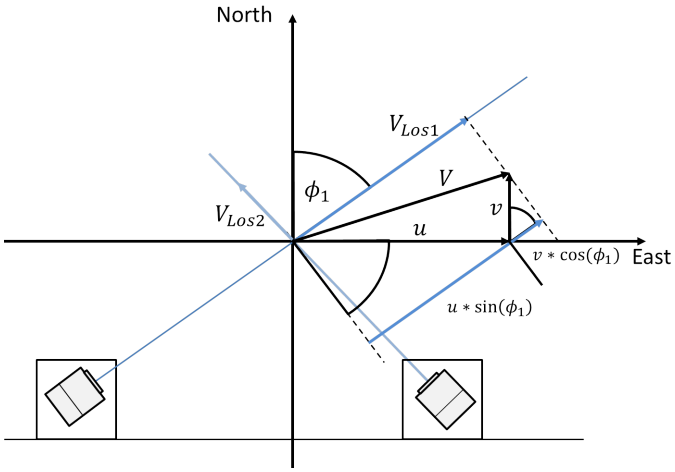

Figure 4: *Estimation of wind vectors with two LiDAR systems. Only the vectors of LiDAR L1. Illustration based on (Trabucchi, 2013).*

2.2 Fundamentals of SAR satellite remote sensing measurements

Satellite-based remote sensing offers the possibility to measure dimensions and various parameter of the earth's surface covering hundreds of square kilometres. In general, radar satellites interpret the backscattered fraction of an emitted radio wave pulse on the earth surface to determine the desired quantity of the observed area. As radio waves in the radar frequency band are widely unaffected by tropospheric phenomena such as clouds, radar satellites are capable to measure independently from weather conditions. Although the usage for radar satellites is manifold the focus of this chapter is on the retrieval of the surface wind speed and the SAR measurement principle. A variety of information about marine applications for SAR satellite remote sensing can be found in the SAR Marine Users Manual by the National Oceanic and Atmospheric Administration (NOAA) (Jackson and Apel, 2004).

2.2.1 SAR satellite measurement method

Radar satellites emit radio pulses with a wavelength λ_r typically in the range of a few centimetres, which are backscattered from the earth's surface. The received backscattered intensity is measured and expressed as the normalized radar cross-section (NRCS) σ_0, which is defined as the logarithmic ratio between received energy at the sensor and the energy scattered in isotropic direction at the surface. The NRCS depends strongly on the incidence angle Θ and tends to decrease with increasing incidence angle (Holt, 2004).

The basic geometric set up for the radar satellite measurements is shown in the Figure 5 below. While travelling through the atmosphere to the ground, the radar beam of satellite is expanding, leading to an illuminated area of several hundred square kilometres in size. Due to the broadening of the radar beam the incidence angles of the transmitted pulse varies over the beam footprint (Moiera, 2014).

To measure the distance to the reflecting surface, the flight time of the radar pulse is

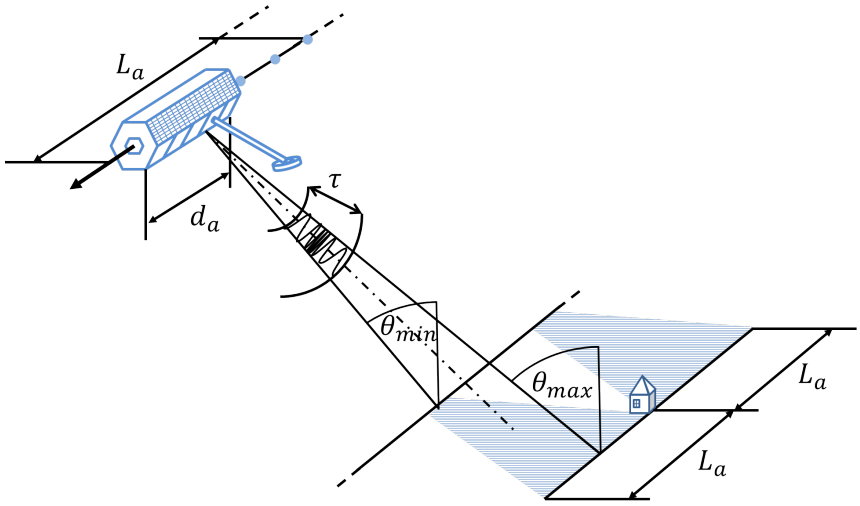

Figure 5: *Measurement geometry for radar satellite. The satellite sends a frequency modulated pulse to the surface, which expands on its way through the atmosphere. A synthetic aperture is formed by summing and weighting the received signals at various position along the Sattelite's flight path. Only the illuminated area at the beginning and end of the synthtic aperture seen by a target is shown. Illustration based on (Moiera, 2014) and (McCandless and Jackson, 2004).*

calculated. In opposition to LiDAR measurements radar satellites receive backscatter from a solid surface and not from air particles along the pulse flight path. The range resolution is strongly connected to the effective pulse width τ of the radar pulse as shown in Equation 7.

$$r_{res} = c \cdot \tau / 2 \tag{7}$$

With typical pulse repetition frequencies around 4 kHz ($\tau \approx \frac{1}{4}$ ms) range resolutions of about 37.5 km are possible. According to Equation 7 a shorter pulse will lead to higher resolutions but will also result in lower transmittable energies, which limits the minimal pulse width. For further improvements of the range resolution SAR systems often use a frequency modulated pulse, a so-called "chirp signal", which is created by slightly changing the frequency of the pulse while it is emitted. The modulation leads to a broader bandwidth of the send radar pulse around its basic wavelength λ_r. As effective pulse width τ and pulse bandwidth β are connected to each other by $\tau = 1/\beta$ a wide bandwidth will lead to a short effective pulse width increasing the range resolution significantly. For example, a linearly modulated chirp signal frequency with a typical SAR pulse bandwidth of 20 MHz will lead to range resolutions around 7.5 m. Depending on the incidence angle Θ the effective resolution at ground r_{gr} can then be found by projection of the range resolution on the horizontal plane as shown in Equation 8, leading to achievable ground resolutions of smaller than 1 m.

$$r_{gr} = r_{res} \cdot sin(\Theta) \tag{8}$$

To determine the direction of the backscattered signal, radar satellites make use of the Doppler effect introduced in Equation 1. Since the satellite orbits the earth with a fixed speed, backscattered signals do either have a positive or negative Doppler shift, depending

on their location in reference to the satellite's moving direction. This is a strong contrast to the LiDAR systems, where the Doppler effect is used to determine the radial wind velocity. The direction resolution ϑ_a depends strongly on the size of the radar antenna d_a, radar wavelength λ_r and range r_a and can be described by Equation 9.

$$\vartheta_a = \lambda_r \cdot r_a / d_a \tag{9}$$

From Equation 9 it can be seen that for high direction resolutions a space born radar satellite must feature a big antenna size, which is not realizable due to transportation and structural limits. SAR satellites overcome this constrains by summing and weighting several emitted radio pulses along a certain distance of the flight track. Considering the orbital speed of the satellite a synthetic antenna with aperture sizes L_a of several kilometres can be formed, improving the direction resolution significantly. In case the amount of emitted pulses to form the synthetic aperture is high, the minimal resolution is not depended on the wavelength and distance any more, but instead can be approximated by the half size of the satellites antenna (c.f. Equation 10).

$$\vartheta_a = d_a / 2 \tag{10}$$

This contrasts Equation 9, as the azimuth resolution now improves with a smaller antenna size. This enables SAR satellites to reach azimuth resolutions down to a few metres. However, the challenge for SAR satellite is to have a system that records, sums and weights the different signals correctly along the flight path of the SAR satellite in order to process the image and to identify the target area. More information about the working principles and derivation of Equation 9 can be found in (McCandless and Jackson, 2004).

2.2.2 Estimation of offshore surface wind speed by radar satellites

As radar satellites only measure the NRCS σ_0, which depends on the structure of the ocean surface, the wind speed and direction can not be derived directly. Instead the surface wind speed is retrieved by careful observation of characteristic surface parameters linked to the wind flow. In this connection radar satellites observe the back scatter originating from capillary waves, which are directly created by the influence of the wind flow over the ocean surface. Capillary waves are small waves with heights in the range of a few cm and occur on the ocean surface even with distinct swell existent, which is illustrated in Figure 5. The wavelengths of the capillary waves are in the same range as the wave length of the radar pulse, whichs leads to Bragg-reflection if the path difference of the radar pulse matches half of the wavelength of λ_r as shown in the following Equation 11

$$\lambda_w = \frac{\lambda_r}{2 \cdot sin(\Theta)} \tag{11}$$

Bragg scattering occurs predominantly at incidence angles between 15 ° to 50 °. For smaller or larger angles back scattering occurs due to smooth surfaces orientated perpendicular to the radio beam at the top or the side of the waves. In addition, the strength of the received Bragg scatter depends also on the capillary wave direction relative to the antenna orientation, which is strongest for waves moving along the orientation of the antenna and weakest for perpendicular moving waves (Holt, 2004).

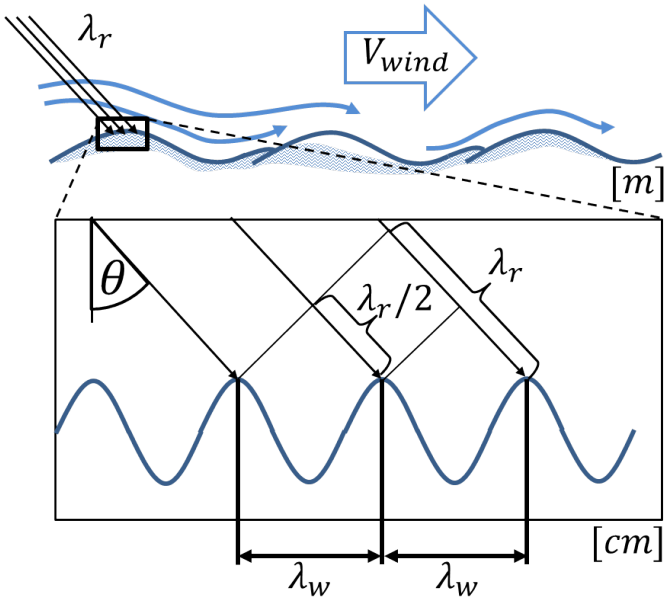

Figure 6: *Bragg scattering of radio waves on capillary waves.*

After having found the NRCS σ_0, a geophysical model is used to predict the relation between the backscatter coefficient and the surface wind speed at 10 m. However, the retrieval of the coefficients for the geophysical model function is not trivial and have to be solved empirically by an algorithm in iterative steps (Ren et al., 2012).

2.3 Vertical wind profile of the marine boundary layer

The vertical wind profile describes the horizontal wind speed in dependency of the height over the ground. Wind boundary layers have mostly been studied onshore, where the friction of the surface can be considered independent from the wind speed. In marine atmospheric boundary layers (MABL) the surface roughness is much lower leading in general to a smaller wind shear and higher wind speeds, but is also depended on the wind speed itself as it invokes waves which alter the surface roughness. In the following Section first a general description of the vertical wind profile is given followed by a more specific explanation of the MABL. A detailed summary about on-and offshore vertical wind profiles is given in (Emeis, 2013).

2.3.1 Logarithmic vertical wind profile

The general shape of the vertical logarithmic wind profile is illustrated in Figure 7 for different atmospheric stabilities. At the ground the wind speed of the vertical wind profile is 0 m/s and initially increases very strongly but tends to increase more slowly with higher heights. At heights above 100 m the horizontal wind speed stabilizes and does not increase further.

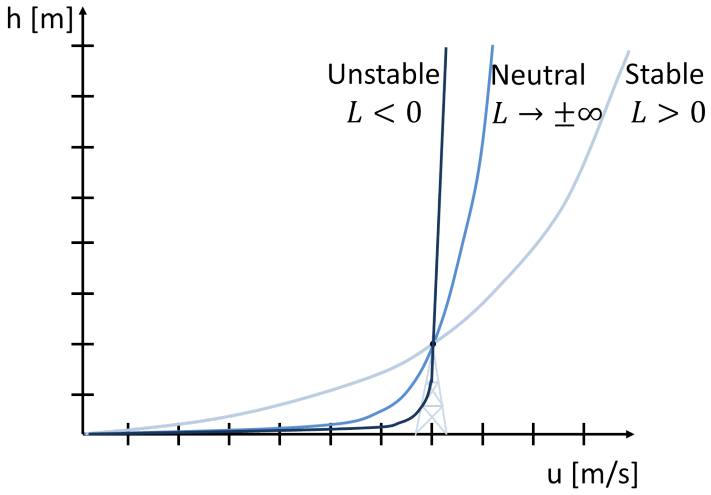

Figure 7: *Logarithmic profiles with measured reference wind speed for different atmospheric stabilities.*

Air-layers relevant for the vertical wind profile can be found in the lower Troposphere (up to 1000 m), which can be further subdivided in the Ekman layer (above 100 m) and the Prandtl layer (until 100 m). In the Prandtl layer viscous friction forces dominate the wind flow and lead to a strong wind shear near to the ground. Moreover the friction forces prevent that the wind flow is deflected by the Coriolis force. At higher heights finally a smooth transition to the Ekman layer takes place. In the Ekman layer friction forces can be neglected and the Coriolis force now becomes a dominant factor. This leads to a change of the direction but only to a small speed up of the wind flow with increasing height. The vertical wind profile can be mathematically described by a logarithmic relationship shown in Equation 12, which is valid for the Prandtl layer on flat terrain.

$$u(z) = \frac{u_*}{k}\left(ln\left(\frac{z}{z_0}\right) - \Psi(z, z_0, L)\right) \tag{12}$$

The factors u_* and z_0 describe the shear stress and the surface roughness length, which do take into account the friction of the surface. The surface roughness length is the height over the ground where the horizontal speed becomes 0 m/s. The correction term Ψ describes the influence of the stability on the atmosphere, which can be stable, neutral or unstable. If one wind speed value of the logarithmic profile $u(z_a)$ is known for example by anemometer

measurement in a certain height z_a, the shear stress parameter u_* can be expressed by the known values of the logarithmic profile in height z_a as shown in Equation 13.

$$u_* = \frac{u(z_a) \cdot k}{ln(\frac{z_a}{z_0} - \Psi(z_a, z_0, L))} \tag{13}$$

The found expression for u_* can then be inserted into Equation 12, delivering the logarithmic profile as a relation to the measured reference wind speed $u(z_a)$ at height z_a as shown in Equation 14 (Lange, 2003).

$$u(z) = u(z_a) \cdot \frac{ln(\frac{z}{z_0} - \Psi(z, z_0, L))}{ln(\frac{z_a}{z_0} - \Psi(z_a, z_0, L))} \tag{14}$$

2.3.2 Stability parameter and marine boundary layer

Atmospheric stability denotes the relation between the change of temperature of the atmosphere to the change of temperature from a rising or falling volume of air. In the simplest case the atmospheric stability is neutral, so that the atmosphere and the air volume always have the same temperature. Because of this, no thermal driven convection takes place in this kind of atmosphere. Neutral conditions do rarely occur and the stability term Ψ becomes zero in this case. For a stable stratification a rising air volume cools down faster than the atmosphere around it, therefore forcing the air volume to stop rising at a fixed height. In comparison to the neutral stratification every vertical movement is damped and prevents a mixing of the atmosphere. This leads to a very strong wind shear with lower wind speeds at the ground and up to 50% higher wind speed in greater heights than under neutral conditions. For unstable stratification, the atmosphere cools down faster than the rising air volume, causing an acceleration of the air volumes when rising or sinking. This leads to a significant mixing of the atmosphere, which leads to a reduction of the wind shear compared to neutral conditions (Emeis, 2013).

To describe the influence of the atmospheric stability on the vertical wind profile a semi-empirically mathematical model was found by Obhukov, which is characterized by the so called Obhukov length L, which is described by the following Equation 15 (Obukhov, 1971).

$$L = -\frac{u_*^3 \cdot T_*}{kg \cdot H_{flux}} \tag{15}$$

In Equation 15 u_* is the frictional velocity, T_* is the virtual potential temperature and H_{flux} is the heat flux between air and surface. The magnitude of the Obhukov length L can be understood as the height, where temperature driven convection becomes dominant over dynamically driven convection. If the ground is warmer than the air the heat flux H_{flux} takes positive values thus heating up the air, which leads to an unstable stratification of the boundary layer. In consequence the Obhukov length will become negative for unstable

and positive for a stable stratification of the atmosphere and is therefore an indicator for the atmospheric condition. If no heat flux is existent L will take infinite values indicating neutral conditions. Found the Obhukov length the stability term Ψ is described by the following mathematical Equations (Badger et al., 2012).

$$\text{Stable}(\text{L} > 0): \ \Psi = -4.7 \cdot z/L \tag{16}$$

$$\text{Unstable}(\text{L} < 0): \ \Psi = \frac{3}{2} \cdot ln\left(\frac{1 + x + x^2}{3}\right) - \sqrt{3} \cdot \arctan\left(\frac{2 \cdot x + 1}{\sqrt{3}}\right) + \frac{\pi}{\sqrt{3}} \tag{17}$$

$$\text{Definition}: \ x = \left(1 - 12\frac{z}{L}\right)^{(1/3)} \tag{18}$$

In opposition to atmospheric boundary layers over ground, the marine boundary layer features much lower surface roughness and frictional velocities, which lead to lower wind shear and higher wind speeds at greater heights. However, over ocean area the wind and waves do influence the roughness conditions of the ocean surface therefore making a logarithmic prediction of the wind profile more challenging. In order to describe the dependency of the surface roughness length on the wind speed in various studies the Charnocks equation has often be applied, which is shown in the following Equation 19

$$z_0 = a_c \cdot (u_*)^2/g \tag{19}$$

The Charnocks parameter a_c was found empirically from measurements and is proposed by Charnock to have a value of 0.0144. However, in other studies the Charnock parameter was found to be 0.02 for near coast and 0.011 for open sea. In addition to the wind driven modulation of the wave height of older waves so called swell can occur, which is not related to the wind speed. The differentiation between young wind generated waves and older swell is necessary, as for young waves the wind speed is faster than the wave speed, resembling therefore the same surface effects as over ground. In opposition the wave speed of swell can be faster than the wind speed, which induces additional vertical movement of the air in the lower air layers, which is not covered by the description of the stability parameter from Obhukov. The wave age c can be expressed by the relation between the phase speed of the waves divided by the frictional velocity of the wind as shown in Equation 20.

$$c_{wave} = c_{ph}/u_* \tag{20}$$

Wave age numbers smaller than 28 can be seen as young waves and as older swell otherwise. From this parameter a first rough check of the validity of the logarithmic approach can be made for free-stream conditions (Emeis, 2013).

In general, the atmospheric stability over offshore area has a trend to be unstable, as air over the oceans surface can be considered as saturated with humidity. Humid air has a slightly lighter density than dry air and therefore tends to rise leading to accelerated vertical movement connected with unstable stratification. Neglecting the effect of humid-

ity on the logarithmic profile might lead to an overestimation in wind speeds of a few percent(Emeis, 2013). Moreover the ocean surface temperature does not show a diurnal cycle as for soil, since the ocean can be considered to have an unlimited heat capacity. Therefore during autumn and winter months often unstable stratification occurs when cold air from land masses flows over the warmer waters of the ocean. On the other hand stable stratification can be found during spring and summer, when warm air flows over the colder waters of the ocean.

2.4 Wind turbine wake

Wakes are a phenomena created when kinetic energy is extracted from the wind flow by the rotor of the wind turbine. In the Figure 8, the general mechanics of wake development are illustrated. By design, the rotor extracts kinetic energy from the incoming airflow, slowing down and reducing the static pressure of the air flow in this process. A cylindrical tube region with a wind speed deficit compared to the non-affected ambient wind forms behind the rotor. Assuming that no air flows across the tube boundary and the air mass within the tube is conserved, Bernoulli's principle is valid and the cross section of the slowed down wind has to expand until the static pressure within the wake equals the static pressure of the ambient flow. The wind speed decrease diminishes gradually, leading to a smooth increase of the wake diameter and therefore the inflow wind speed at the rotor is already lower than the ambient wind speed (Burton et al., 2011).

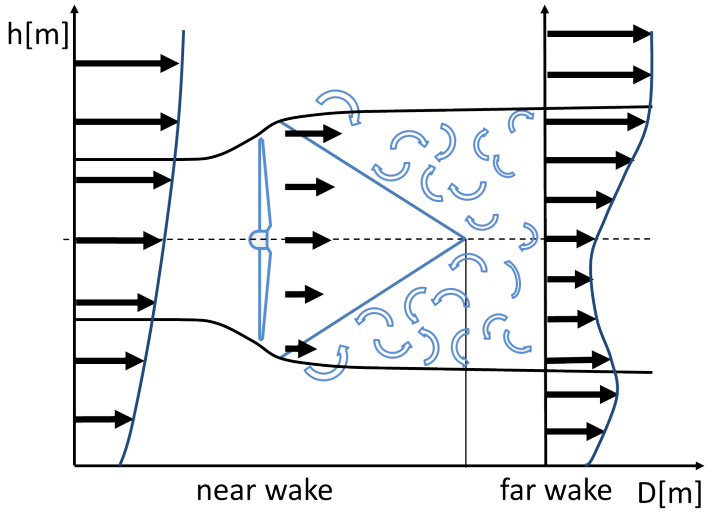

Figure 8: *Wake development behind wind turbine. Two vertical profiles located before and behind the rotor disk are shown. The shear layer thickness is marked by the blue lines. Illustration based on (Sanderse, 2009).*

In addition to the wind speed reduction a tangential component is added to the air flow when passing the rotor leading to a wake rotation. This effect is a reaction of the torque acting on the wind turbine, which requires an equal torque in opposite direction acting on the air flow. The tangential acceleration occurs over the thickness of the blade with no tangential velocity upstream of the turbine and maximum tangential velocity immediately

downstream of the rotor (Burton et al., 2011). In reality the assumptions mentioned in the beginning of this chapter are not fully valid. Due to the wind speed gradient between wake and ambient wind speed, a shear layer as marked by the blue lines in Figure 8 forms, intensifying with downstream distance. This layer leads to a turbulent mixing of lower wind speeds with higher ambient wind speed and finally enables a recovery of the wake to ambient wind speed after greater distances. A distinction in near wake and far wake can be made at the point were the thickness of the shear layer reaches the height of the rotor hub, which happens approximately in 2 to 5 rotor diameter distance. In near wake most of the wake expansion takes place and the shear layer is not fully developed, leading almost to a rectangular shape of the wake deficit behind the rotor area. In far wake the mixing layer is fully developed and the wind velocity and turbulence distribution change smoothly to a Gaussian shape. By definition the far wake ends at large distances with 8 - 10 rotor diameter distance. It has to be mentioned that the turbulent intensity is transported in far greater distances of up to 15 rotor diameters. The shape of the wake mainly depends on the rotor design, thrust and also on the atmospheric conditions (Iungo and Porté-Agel, 2014), particularly considering the logarithmic shape of the vertical wind speed profile as shown in the Figure 8. The vertical profile can be superposed with the normal wake development, leading to a shift of the maximum wake deficit from the hub height level downwards (Sanderse, 2009).

3 Material and Methods

3.1 Description of experimental set-up and dataset

The experiment is a cooperation between ForWind in Oldenburg and the DLR in Bremen and was carried out at the offshore wind farm *alpha ventus* located in the German North Sea. Measurements from LiDAR and radar satellite were made simultaneously with each system providing individual wind field information around and inside the offshore wind farm. In total four datasets have been measured during January 2014.

3.1.1 Experimental set up

For the experiment three *Leosphere Windcube 200s* Doppler LiDAR systems have been deployed and operated by ForWind on platforms at the *alpha ventus* wind farm. Two systems were stationed on the research platform and meteorological mast FINO1 at the westerly side of the wind farm, while the third LiDAR device was installed on the substation AV0 on the south easterly corner of the wind farm (cf. Figure 9).

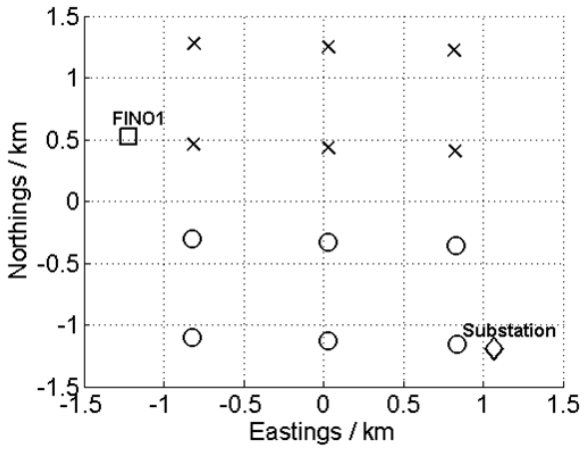

Figure 9: *Experimental layout at the alpha ventus wind farm. The turbine position of type Senvion 5M (×) and Areva Multibrid M5000 (○) are marked. Two LiDAR systems were stationed on the FINO1 platform (□) and one system on the substation (◇).*

The systems have been levelled using the sea surface as a reference and azimuth and elevation angles have received a correction for the database entry accordingly. For easier identification the LiDAR systems on the FINO1 platform are labelled LiDAR1 and LiDAR3 and the system installed on the substation is referred as LiDAR2 in the course of this thesis. LiDAR measurements were carried out in a so called PPI (**P**lan **P**osition **I**ndicator) scan mode with a small fixed elevation angle and 360 ° azimuth turn excluding sections with blocked sight. Elevation angles have been 1.6 °, 0.8 ° and 0.5 ° for LiDAR1, LiDAR2 and LiDAR3, respectively. The scan trajectories were not synchronized with each LiDAR system scanning the wind field individually within a radius of 6 km around the installation location. The LiDAR systems emit pulsed laser radiation with a wavelength $\lambda = 1540\,\text{nm}$ and are able to turn the beam 360 ° in azimuth with a 0.1 ° increment step. The maximum measurement distance is around 6 km with a minimal possible spa-

tial resolution of 50 m (Leosphere, 2012). The settings of the LiDAR systems used for the measurement campaign are summarized in the Table 1.

Table 1: LiDAR Parameters

Parameters	Value	Unit
Wavelength	1540	nm
Pulse repetition rate	10000	Hz
Pulse duration	400	ns
Accumulation time	1	s
Samples per range gate	128	-
Number of range gates	198	-
Range gate centre distance	30	m
Max/Min range	5970/60	m
Scanner turning speed	1	deg/s
Azimuth and elevation resolution	0.1	deg
Measurement error V_{Los}	0.5	m/s

Radar observations were provided by the satellite TerraSAR-X (TS-X) operated by the DLR. TS-X utilizes radio waves in the X-band with a wavelength λ_r of approximately 3 cm and make use of the SAR principle to achieve high image resolution down to one metre (see Section 2.2.1). TS-X features three different modi with varying area coverages and image resolutions. In *Spot Light* mode the satellite focus its radar antenna on an area with approximately 100 square kilometres in size and resolutions of one to three metres. In *Strip Map* mode the satellite covers a rectangular area with several hundred of square kilometres in size and resolutions of 3 m. The third possible mode is the *ScanSAR* mode with an even higher area coverage of several thousands of square kilometres with a more rough resolution of 16 m (Fritz and Eineder, 2008). In order to cover the power demand of the instruments, TS-X orbits the earth on a sun synchronous path at the dawn/dusk line of the earth. Because of this orbit, observations of a specific area can only be made around the time of dawn and dusk, therefore limiting the maximal possible number of observations. In addition to the intensity information of the transmitted pulse, TS-X is also able to derive the phase shift information contained in the received signal, therefore allowing to access additional information about the composition of the observed surface (Fritz and Eineder, 2008). In the Table 2 the parameter used for TS-X on the different measurement dates are summarized.

3.1.2 Description of dataset

In Figure 10 an example of the scan trajectory of the LiDAR systems is shown, which represents the measurement trajectories used on the other dates. One complete scan for all LiDAR systems is plotted, where each mark displays the position of a range gate center. It has to be mentioned that the vertical axis is not in equal scale with the x and y axes. It can be noticed that the PPI scan of the LiDAR trajectory is not perfectly planar, but has a small elevation angle leading to a conical scan instead. Therefore the measurement height

increases with the radial distance to the LiDAR system from 25 m to 180 m, depending on the LiDAR system. In addition, a tilt of the conical scan especially for LiDAR2 can

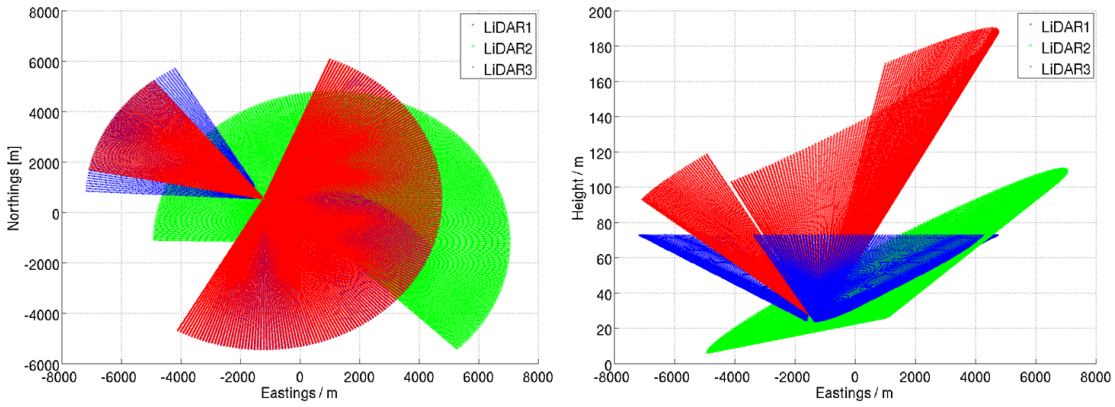

Figure 10: *LiDAR trajectory for one scan. Shown are the positions of the range gate centers of the different LiDAR systems. Note that the scale of the vertical axis is not equal to the scale of the x and y axes.*

be noticed. Due to the conical scan, the overlapping measurement area is relatively small and thus an evaluation of wind fields in terms of multi-LiDAR measurements is limited to those areas. Moreover the LiDAR installed on the FINO1 platform do almost have the same location, which will lead to similar viewing angles and in consequence to a high error in the estimation of V when just these systems are considered for multi-LiDAR usage. Therefore only the LiDAR2 on the substation together with at least one LiDAR on the FINO1 platform should be used for multi-LiDAR evaluation.

Four wind field acquisitions were made by TS-X on the 16.01, 17.01, 19.01 and 22.01, respectively. Measurement times have been 6:00 (UTC) on three dates and 17:27 (UTC) on the 19.01., respectively. Satellite observations have been made in *SpotLight* mode on all dates except on the 22.01 where the *StripMap* mode was used. Depending on the used mode the scanned area was approximately 10 km×10 km or 30 km×30 km in size with varying incidence angle between 30 ° to 50 °. From the radar picture wind fields with 1 m resolution in x and y direction can be theoretically obtained, but which will result in less accurate and noisy wind field measurements. For this purpose wind fields from TS-X have been downsampled by the DLR to a horizontal resolution of 60 m, which corresponds bet-

Table 2: TS-X Parameter

Parameter	16.01.	17.01.	19.01.	22.01.	Unit
Modus	Spot Light	Spot Light	Spot Light	Strip Map	-
Time	05:59	05:42	17:27	05:51	hh:mm UTC
Wavelength	3	3	3	3	cm
Scene Size	10x12	10x12	10x12	28x31	km
Incidence Angle	28	49	51	38-40	deg

ter to the resolutions achievable with the LiDAR measurements. In Figure 11 an example of a radar backscatter map from TS-X is shown for the 22.01.2014. It can be noticed that the radar picture is slightly rotated, resulting from the satellites flight path. The wind farm *alpha ventus* can be seen as a cluster of white dots in the upper left corner, illustrating the high spatial coverage possible with radar satellites.

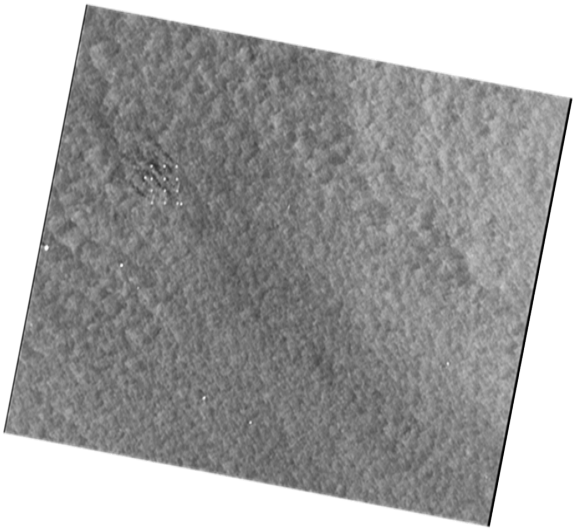

Figure 11: *Radar backscatter map from TS-X on the 22.01.2014. The windfarm alpha ventus can be seen in the upper left corner.*

3.1.3 COSMO-DE data

For additional information on the state of the atmosphere on the measurements dates additional analysis data from the COSMO-DE mesoscale weather model of the German Weather Service (DWD) was used. The COSMO-DE model is able to simulate meteorological data on short time scales up to 21 hours with 1 hour time step and a grid resolution of 2.8 km. COSMO-DE periodically updates the weather simulation every 3 hours by assimilation of available measured meteorological data from different sources. The weather model can be used either for short time prediction of the atmospheric state, or for simulation of previous weather conditions based on archived meteorological data. The latter method differs from a weather prediction, as for each time step real meteorological data is integrated in the model and only the overall weather state at the time step zero is simulated, thus allowing a good estimation of the atmospheric conditions. However, deviations between measured and simulated reanalysis data have to be considered since the simulation gives a fit of the weather situation over a larger area but not at a specific point. A description of the COSMO-DE weather model and its parameters is given by (Baldauf et al., 2009).

Within this master's thesis different atmospheric parameters are used from the COSMO-DE model, which are given as instantaneous values at the hourly time steps. Data used

Table 3: Atmospheric parameter from COSMO-DE

Parameter	16.1	17.1	19.1	22.1	Unit
Wind speed at 73 m	11.8	13.1	14.9	8.7	m/s
Wind direction at 73 m	174.5	175.3	125.4	134.9	deg
surface roughness z0	$2.19 \cdot 10^{-4}$	$2.45 \cdot 10^{-4}$	$3.67 \cdot 10^{-4}$	$1.23 \cdot 10^{-4}$	m
Ocean temperature	280.3	280.1	280.2	280.2	K
2 m Air temperature	278.5	280.1	277.7	275.2	K

from the model are the wind speed components U and V, the roughness length z_0 and the 2 m air Temperature T_{2m} as well as the ocean surface temperature T_S. In the Table 3 the parameters given by COSMO-DE for the different dates are summarized.

3.2 Applied algorithms

For some steps of the processing procedure presented in this thesis, algorithms developed at ForWind and DLR have been applied, which will be described briefly in this chapter. Algorithms used for this master's thesis are MuLiWEA (Multiple-LiDAR Wind Field Evaluation Algorithm) developed at ForWind (van Dooren, 2014) and XMOD2 developed by DLR (Li and Lehner, 2014).

3.2.1 MuLiWEA

The algorithm MuLiWEA is able to perform an analysis of the wind field measured by multiple LiDAR systems in Plan Position Indicator (PPI) mode. To calculate the wind field, MuLiWEA defines a planar Cartesian mesh grid of customisable size within the area of interest. Around each centre of the defined grid v_{los} measurements from different LiDAR systems are selected within a certain radius of influence R for the evaluation of the absolute wind speed according to formula 6. Values closer to the grid points are given more weight for the calculation by applying a Cressmann function, which gives full weight to values at the centre and zero weight at the border of the evaluation radius R. The optimal distance d of the grid cell centres is connected to the achievable spatial resolution of the LiDAR systems, while for the optimal radius R is assumed to be $R = d/\sqrt{2}$, delivering full area coverage for the Cartesian grid. As the PPI scans are not perfectly planar and thus values can occur in different height sections, the evaluation radius is expanded in z direction forming a cylinder within values are considered for the retrieval of the wind speed components at the centre of the cylinder. It has to be mentioned that no weighting is applied in z direction. In the Figure 12 the mesh grid showing the grid centres for selection of valid LiDAR values applied by MuLiWEA is illustrated. In addition to the weighting along the radius of influence also a weight is applied on each LiDAR system depending on the amount of values available within each grid cell. LiDAR systems with a lower amount of values available in a grid cell have a higher weight than LiDAR systems with a higher amount of values.
Furthermore MuLiWEA is able to track wakes behind wind turbines and able to deliver the shape of the wind speed profile in wake at various position downstream of the wind

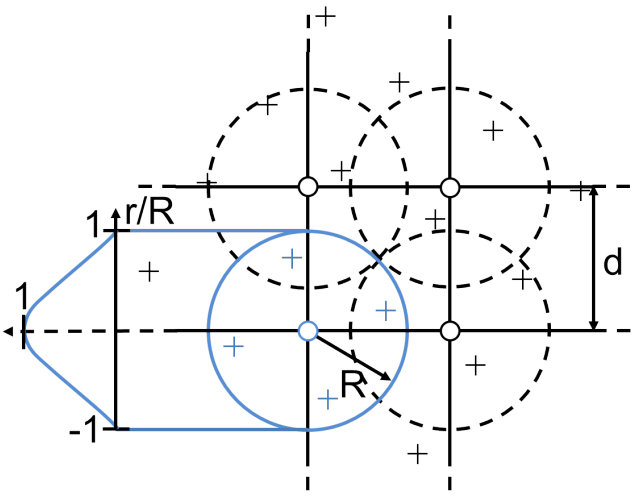

Figure 12: *MuLiWEA grid for estimation of the wind speed components u and v at the grid centre highlighted in blue. V_{Los} values closer to the centre are given more weight by a Cressman function. Shown is the optimal area usage with an evaluation radius of $R = d/\sqrt{2}$ around the grid centres. Illustration based on (van Dooren, 2014).*

turbine. Finally, MuLiWEA provides the single measurement dual-LiDAR direction error for every grid cell point. In this Section only a brief overview of the most important features of MuLiWEA could be given. The full description of MuLiWEAs functions and usages are described in (van Dooren, 2014).

3.2.2 XMOD2

XMOD2 is an algorithm for the estimation of the surface wind speed in 10 m height from backscattered satellite radar pulses in the X-Band developed by the DLR. The general approach of the algorithm is to solve a Geophysical Model Function (GMF) iteratively. XMOD2 makes use of a non-linear GMF with the general form as shown in Equation21

$$\sigma_0(U_{10}, \theta, \phi) = B_0^p(U_{10}, \theta)(1 + B_1(U_{10}, \theta)cos\phi + B_2(U_{10}, \theta)cos2\phi) \tag{21}$$

where U_{10}, θ and ϕ are the wind speed at 10 m height, the incidence angle and the relative angle between antenna look direction and wind speed. The parameter p is constant with a value of 0.625 (Li and Lehner, 2014). The coefficients B_0, B_1 and B_2 have been determined empirically by systematic adjustment of the coefficients until the evaluated backscattered radar cross section from formula 21 equals the backscattered radar cross section σ_0 detected by TerraSAR-X. For this purpose a tuning dataset, consisting of buoy measurements extrapolated to 10 m height by applying a neutral logarithmic vertical profile was used. With the coefficients known, the equation 21 delivers a direct relation between detected radar cross section σ_0 and 10 m wind speed U_{10}. Validations between in situ buoy measurements and the corresponding 10 m wind speed retrieved by XMOD2 do show a fixed bias of -0.29 m/s and a mean root square error of 1.46 m/s between the two datasets.

In order that XMOD2 can deliver a good wind speed estimate, the backscattered sig-

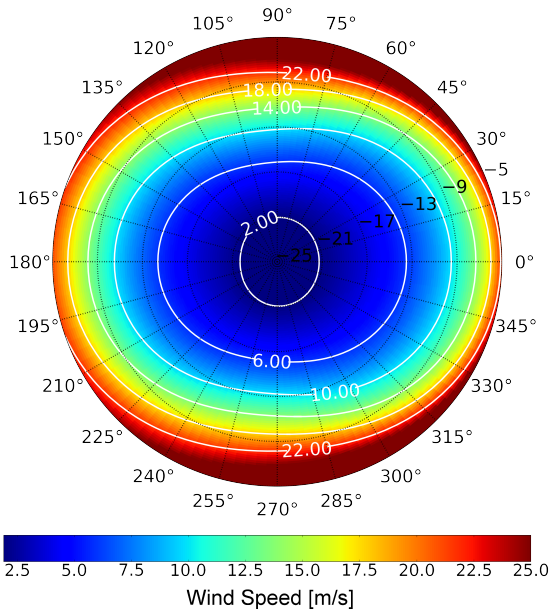

Figure 13: *Output of XMOD2 algorithm for an incidence angle of* 35 °. *The angles represent the relative angle between antenna look direction and real wind speed. Radial black lines do show the amount of radar backscatter in dB. The wind speed is color coded and contours of same wind speed are shown by white lines. Note that the contours are elliptic due to the sinusoidal change of radar backscatter with relative view angle* ϕ.

nal must be strong enough to be distinguishable from the background radar noise. The backscattered signal strength itself is a function of the real wind speed at 10 m height, the incidence angle θ and the relative wind direction ϕ. In general the backscattered signal strength increases with steeper incidence angles, but is limited to an angle window of approximately 20 ° to 45 ° as Bragg scattering does predominantly occur in this range. In addition the relative wind direction adds a sinusoidal behaviour to the backscattered signal strength with best signal quality for upwind/downwind cases and lowest for crosswind situations. This effect is caused by the wave direction of capillary waves, which changes with wind direction. For upwind and downwind cases the wave front is orientated perpendicular to the incoming radio pulse leading to strong Bragg Scattering. The opposite case occurs for crosswind situations with weaker Bragg scattering. Errors in the wind speed calculation are mainly attributed to phenomena altering the ocean surface such as oil spills or strong rain but can be also caused by errors of the tuning dataset itself, especially due to the logarithmic extrapolation assuming a neutral vertical wind profile. An overview of the output of XMOD2 is shown in the Figure 13 for a fixed incidence angle of 35 ° (Li and Lehner, 2014).

3.3 Data processing

The datasets of LiDAR and TS-X exhibit fundamental differences in the spatial- and temporal distribution, especially the height level. To allow a comparison between LiDAR and TS-X data, a processing algorithm was developed within the scope of this thesis. It has to be mentioned that a processing of the different measurement times of the wind fields was not carried out because of complexity and would go beyond the scope of this thesis. In Figure 14 the four major processing steps of the algorithm are shown.

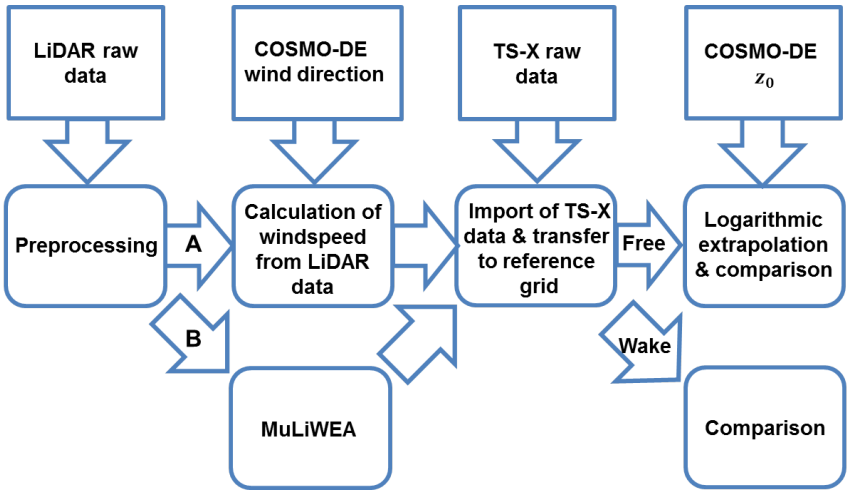

Figure 14: *Flow chart of the processing algorithm. Processing steps are shown in rounded boxes. Imported data is shown in cornered boxes.*

After preprocessing of the LiDAR raw data the horizontal wind speed V is calculated either for single LiDAR data using additional wind direction information from COSMO-DE or directly from multi LiDAR data using MuLiWEA (c.f. Section 3.2.1. In the next step the wind field data of TS-X is imported and the different spatial distributions of LiDAR and TS-X data are processed by a transfer to a common reference grid. In free stream conditions an additional height extrapolation of LiDAR data down to the height level of TS-X is performed before the actual comparison is carried out.

3.3.1 Preprocessing

First LiDAR data is imported from the ForWind database with a maximal time lag of 120 seconds to the satellite measurement, representing one complete PPI scan. As a criterion of data quality the CNR value (see also Section 2.1.2) was checked for every LiDAR system. Measurements with too low CNR are not expected to provide meaningful data and need to be filtered. A guideline from the manufacturer Leosphere (see Equation 22) is used for the estimation of too low CNR values for the *Windcube200s*,

$$CNR(t_{ac}, f_p, N_{fft}, t_p) = -27dB - 4\log_{10}\left(\frac{t_{ac}f_p}{10000}\right) - 4\log_{10}\left(\frac{N_{fft}}{128}\right) - 4\log_{10}\left(\frac{t_p}{400}\right) \tag{22}$$

where t_{ac} represents the accumulation time, f_p the pulse repetition frequency, t_p the pulse duration and N_{fft} the number of samples per range gate for the calculation of the Fourier spectrum. Using the parameter shown in the Table 1 a minimal CNR value of $-27\,\mathrm{dB}$ is found. Since CNR values close to this limit can already show reduced data quality the minimal limit was increased to $-22\,\mathrm{dB}$. Also very high CNR values can occur by strong back reflection on obstacles such as wind turbines, which lead to invalid line of sight velocity readings. As a criterion for too high CNR values the highest natural occurring CNR value at the focus range of the LiDAR beam (Cariou and Boquet, 2010) is taken as reference and a simple filter is applied neglecting all CNR values higher than this value. However, not all bad CNR values can be detected by this approach but the remaining number is very small compared to the total available amount of measurements. In Figure 15 the effect of the CNR filtering on the LiDAR dataset is shown. Note that bad CNR values occur frequently in great distances and behind sight blocking structures.

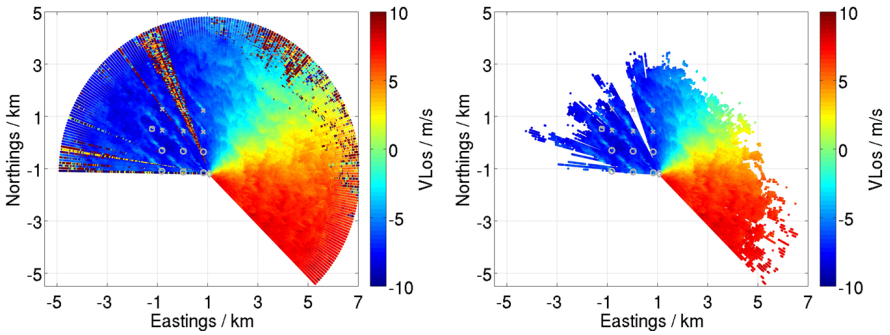

Figure 15: *(left) Unfiltered scan of V_{Los} values. (right) CNR filtered scan of V_{Los} values. Measurements were taken by LiDAR2 on January 22.*

3.3.2 Calculation of horizontal wind speeds from LiDAR data

The horizontal wind speed can either be calculated from single LiDAR measurement data or from multi-LiDAR data using MuLiWEA (c.f. Section 3.2.1). For measurements with a single LiDAR system the horizontal wind speed is calculated by transformation of the V_{Los} measurements on the wind direction (c.f. Equation 3) obtained from the weather model COSMO-DE at the centre of the wind farm. The relative elevation angle δ in Equation 3 is neglected as the elevation angles of the LiDAR where always smaller than ($< 1.57\,^\circ$) and the equation can be simplified by Equation 23.

$$V = \frac{V_{Los}}{\cos(\alpha)} \tag{23}$$

The relative angle α can be expressed as the difference $\Phi - \vartheta$ between the azimuth angle Φ of the LiDAR and the wind direction angle. The method delivers reasonable results for small deviations between Φ and ϑ, but tend to produce larger deviations with $|\alpha|$ approaching values of $90\,^\circ$ (c.f. Section3.4). Therefore LiDAR measurements with relative errors larger than 15% are not considered in the further calculation process, which roughly corresponds to sectors with $|\alpha| > 40\,^\circ$. In Figure 16 the absolute wind speed field calculated

from single-LiDAR measurements is shown for LiDAR2 on January 22. The error of the projection method is further discussed in Section 3.4. For multi-LiDAR data the MuLiWEA algorithm described in Section 3.2.1 is used.

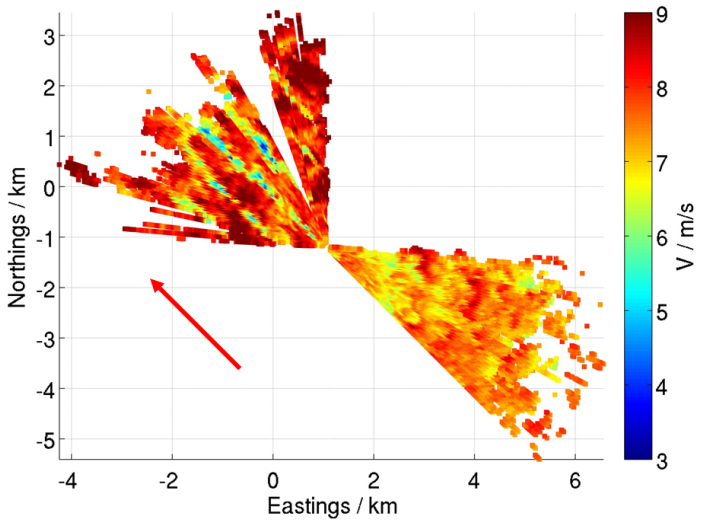

Figure 16: *Horizontal wind speed V calculated by transfer of single LiDAR line of sight values on the real wind direction. The mean ambient wind direction from COSMO-DE is indicated by a red arrow. Sectors with relative errors σ_V/V >15% are filtered and not considered for the further analysis.*

3.3.3 Import of TS-X data and transfer to reference grid

From TS-X measurements wind fields in 10 m height with a resolution of 60 m in x and y direction are derived using the XMOD2 algorithm developed by (Li and Lehner, 2014). As an example the wind field derived by XMOD2 on January 22 is shown in Figure 17. At the location of the wind turbines and other offshore structures high wind speed values due to strong radar backscatter can be observed, which are removed manually around the wind turbines. Since the spatial distribution of LiDAR and TS-X data is different, data is transferred to a reference grid. In case of single LiDAR measurements a polar reference grid with a resolution of 60 m in radial and 1 ° in azimuthal direction is defined around the position of the LiDAR. Wind speed values of LiDAR and TS-X are both transferred to the position of grid cell centres of the polar reference grid. To transfer the LiDAR data all height levels and wind speed values V within a grid cell of the reference grid are replaced by an average of the data at the centre position of the corresponding grid cell. For multi-LiDAR the Cartesian grid applied by MuLiWEA is used as the reference Grid with a resolution of 60 m in x and y direction. Afterwards also the TS-X data is transferred to the location of the grid centres of the reference grid by linear interpolation. In wake conditions both LiDAR and TS-X data are both transferred to a Cartesian grid instead, which is further described in Section 3.3.5.

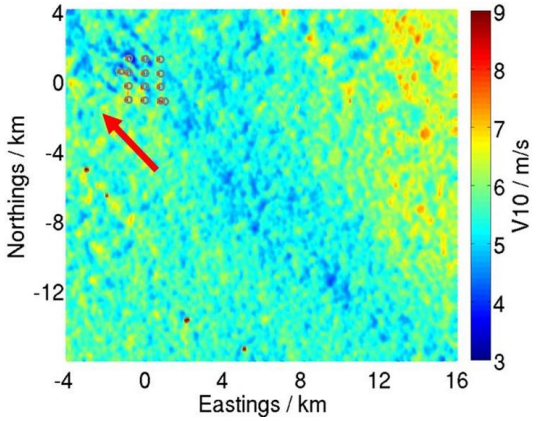

Figure 17: *TS-X 10 m wind field on January 22 calculated with XMOD2. Wake structures can be seen behind the wind turbines. The red arrow indicates the wind direction from COSMO-DE.*

3.3.4 Height extrapolation and comparison in free stream

In order to process the different height levels between TS-X and LiDAR data, a height extrapolation of the LiDAR values down to the height level of TS-X at 10 m above the mean sea surface is carried out assuming a logarithmic vertical wind profile. As dependable data on the state of the atmospheric stability was not available, a neutral logarithmic vertical wind profile is applied (c.f. Section 2.3.1) for the comparison as shown in Equation 24.

$$U(z) = u(z_r) \cdot \frac{\ln(z/z_0)}{\ln(z_r/z_0)} \tag{24}$$

The surface roughness parameter z_0 is obtained from COSMO-DE data at the centre position of *alpha ventus* for the nearest time step to the satellite measurements. The measurement height and wind speed from the LiDAR values are taken as reference height z_r and reference wind speed $u(z_r)$. The error of the extrapolation is further discussed in Section 3.4. After the extrapolation, wind fields from LiDAR and radar satellite can be compared directly. To ensure that only values in free stream conditions are considered, sectors with perturbed wind speed values in and downstream of the wind farm *alpha ventus* are excluded. In free stream conditions wind speed variations are homogeneously distributed and can be approximated by a Gaussian function (c.f. Appendix A) if the size of the averaged area is sufficiently large. Therefore it is possible to describe the characteristic of the wind fields by a mean and a standard deviation. As a first part of the comparison the areal mean of the deviation between the wind fields is calculated by subtraction of the wind fields and a subsequent spatial average and spatial standard deviation in x and y direction for every measurement date. The determined values are also compared to the areal mean of the deviation between LiDAR and TS-X to the 10 m ambient wind speed from COSMO-DE taken at the centre position of the wind farm for the closest time step to the satellite measurements. Secondly, the agreement between wind field structures seen in TS-X and LiDAR data is investigated. Due to the measurement principle of the LiDAR, the measurement time for values along a radial beam of the reference grid is the same,

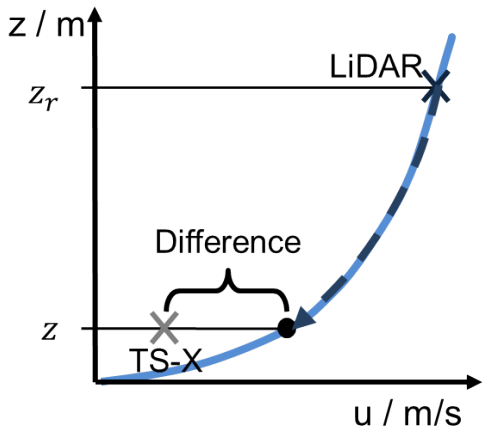

Figure 18: *Logarithmic height extrapolation and comparison. The wind speed values of LiDAR are extrapolated to the height level of TS-X using a logarithmic profile. The remaining difference between the extrapolated LiDAR values and the corresponding TS-X value is used for further comparison.*

while TS-X has a fixed measurement time for every value on the reference grid. Therefore the agreement of wind field structures in dependency on the time lag is investigated by beam wise linear correlation of values from LiDAR and TS-X.

3.3.5 Wake tracking

In wake conditions the assumption of a logarithmic wind profile is not valid and a height extrapolation of LiDAR data is not meaningful. Therefore the investigation is limited to compare wind fields at different height levels with special focus on the location of the wakes seen in LiDAR and TerraSAR-X measurements. The wake tracking algorithm used in this thesis is based on Gaussian fitting of the wake path at various positions downstream of a wind turbine. For this purpose the algorithm interpolates LiDAR and TS-X data on a Cartesian grid downstream of the wind turbine and plots the wake profile along the grid intersections perpendicular to the wake path as shown in Figure 19. For this procedure the approximate direction of the ambient wind speed is needed, which is taken from COSMO-DE data. In far wake (downstream distance $> 4\,\mathrm{D}$) it is possible to approximate the wake velocity profile by a negative Gaussian function (c.f. Section 2.4), which minimum marks the wake centre. The negative Gaussian function is defined in Equation 25,

$$G(x) = -\frac{A}{\sqrt{2\pi\sigma^2}} \cdot e^{-\frac{(x-l)^2}{2\sigma^2}} + C \tag{25}$$

where x is the lateral distance along the intersection from the wake centre l of the Gaussian function. C denotes the original value of the ambient wind speed taken from COSMO-DE. The standard deviation σ describes the width of the Gaussian shape and A the maximal velocity deficit at the centre. The parameters are determined by fitting the Gaussian function to the wake profile by a least squared method. In Figure 25 an example of a wake tracking downstream of a wind turbine in $4\,\mathrm{D}$ to $17\,\mathrm{D}$ distance is shown.

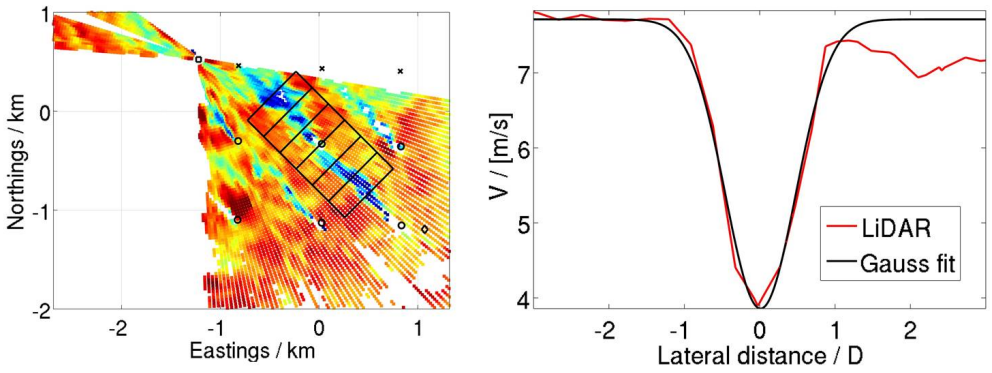

Figure 19: *Illustration of the wake tracking principle. (left) A Cartesian grid (black lines) is defined downstream of the wind turbine AV12. (right) Wake profile (red) extracted by linear interpolation in 6 D distance behind the wind turbine AV12. A least squared Gaussian fit (black) is added.*

3.4 Error estimation

In this Section the major underlying assumptions and errors involved for the processing steps are highlighted and discussed. Major sources for errors are caused by the calculation of wind speed data from single LiDAR systems and the height extrapolation in free stream. It has to be mentioned that errors caused by the transfer and interpolation to the reference grid are neglected here.

3.4.1 Wind speed calculations from LiDAR data

The absolute error of the wind speed calculation for a single LiDAR can be estimated by error propagation of Equation 23 as shown in Equation 26.

$$\sigma_V = \left|\frac{1}{\cos(\Phi-\vartheta)}\right| \Delta V_{Los} + \left|\frac{V_{Los}\sin(\Phi-\vartheta)}{\cos^2(\Phi-\vartheta)}\right| \Delta\Phi + \left|\frac{-V_{Los}\sin(\Phi-\vartheta)}{\cos^2(\Phi-\vartheta)}\right| \Delta\vartheta \qquad (26)$$

The absolute error is composed of the line of sight error ΔV_{Los}, the azimuth error $\Delta\Phi$ and the wind direction error of COSMO-DE $\Delta\vartheta$. The line of sight error is a characteristic of the LiDAR system and can not be avoided. For the *Windcube 200S* a maximum line of sight error of $\Delta V_{Los} = 0.5\,\mathrm{m/s}$ is stated by the manufacturer (Leosphere, 2012). Due to the change of the azimuth angle during the measurement trajectory a further azimuth angle error has to be considered. This error tends to increase with increasing scanner speed. During the measurements the LiDAR operated in the limits recommended by the manufacturer thus achieving a small azimuth error of $\Delta\Phi = 0.1\,^\circ$. For projection of measurements from single-LiDAR, additional wind speed information from the COSMO-DE model is used. Regarding the COSMO-DE model the error cannot be assessed easily, since the simulations are based on multiple numerical models each involving an individual measurement error. The direction error is assumed to be of the same order for as wind vanes $\Delta\vartheta = 4\,^\circ$, since COSMO-DE takes real measurement data as basis for its simulation. A detailed overview into the mechanics of the measurement error is given by (Stawiarski et al., 2013).

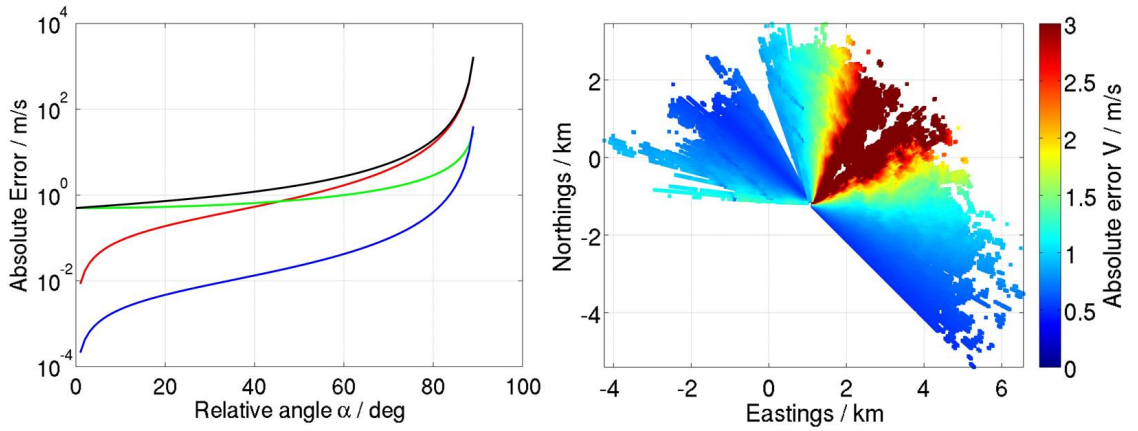

Figure 20: *Absolute error of LiDAR data. (left) Error terms of the absolute error for fixed V_{Los} of 7 m/s; (blue) $\Delta\Phi$; (red) $\Delta\vartheta$; (green) ΔV_{Los}; (black) Sum of error terms.(right) Absolute error of wind field measured by LiDAR2 on January 22.*

However, it was found that the assumed direction error matched for the dates considered in this work, but larger errors can occur especially on other meteorological situations, which are difficult to solve numerically. Based on Equation 26 the absolute error σ_V is plotted in Figure 20. It can be seen that the absolute error increases strongly with increasing values for α. Especially the error term of the wind direction $\Delta\vartheta$ has a strong influence on the absolute error and increases with the measured line of sight velocity V_{Los}. Therefore relative errors σ_V/V >15% are excluded from the comparison process.

3.4.2 Height extrapolation

The validity of the logarithmic model of the vertical wind profile is checked plotting all measured LiDAR and TS-X data over the height (c.f. Figure 21). The vertical profile of the LiDAR data shows a high variability, which can be attributed to the spatial distribution and the measurement error at high values of α. On the 19.01. a trend to a logarithmic shape can be noticed as the fitted neutral logarithmic profile stays within the standard deviation of the LiDAR and TS-X data. However, a complete investigation of the validity of the logarithmic shape could not be given as wind speed values in the lower height levels with strong shear were not available. A further significant error can be attributed to the assumed neutral logarithmic wind profile since neutral stratifications of the atmosphere are rarely existent. In fact the sea and air temperature obtained from COSMO-DE (cf. Table 3) indicate a trend to unstable conditions with strongest instability on the 22 of January. To estimate a maximum deviation between an unstable and neutral profile a constant wind speed with height equivalent to typical conditions during maximum instability (well-mixed boundary layer) is compared to a neutral profile which is indicated by the vertical black line in Figure 1. The maximum deviation between a neutral and unstable profile at 10 m height is estimated to be 16% of the corresponding non extrapolated wind speed measured by the LiDAR. It is worth to mention that the present vertical profiles were not fully unstable and the maximum error is not likely to be reached. Regarding possible

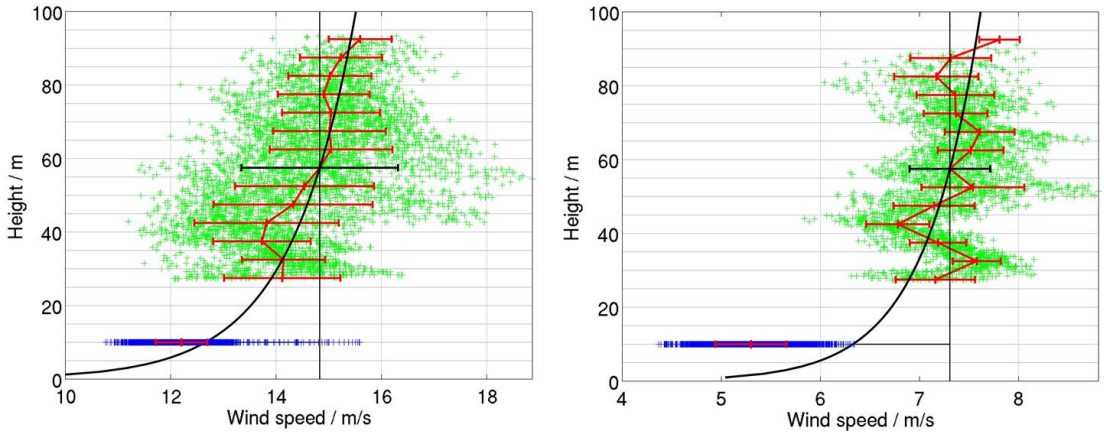

Figure 21: *Vertical distribution of wind speeds using all measurement values of LiDAR2 and TS-X on January 19 (left) and 22 (right) for free stream sector. Mean values and standard deviation of LiDAR data (green) and TS-X data (blue) are calculated in* 5 *m height intervals (red marker and lines). A neutral logarithmic profile using the averaged LiDAR value at* 57.5 *m as reference is plotted with* z_0 *obtained from COSMO-DE.*

stable atmospheric cases higher deviations have to be taken into account, since the wind speed increase between the lowest and maximum height level of typical rotor diameters can reach up to 150% (Emeis, 2013).

4 Results and Discussion

4.1 Free stream conditions

Figure 22 shows the processed and extrapolated wind fields of LiDAR2 and TS-X obtained on two different measurement dates. The spatial average and standard deviation of each wind field is displayed. The wind fields of the remaining measurement days are shown in Appendix B. Results presented in this Section are mainly focussed on measurements ob-

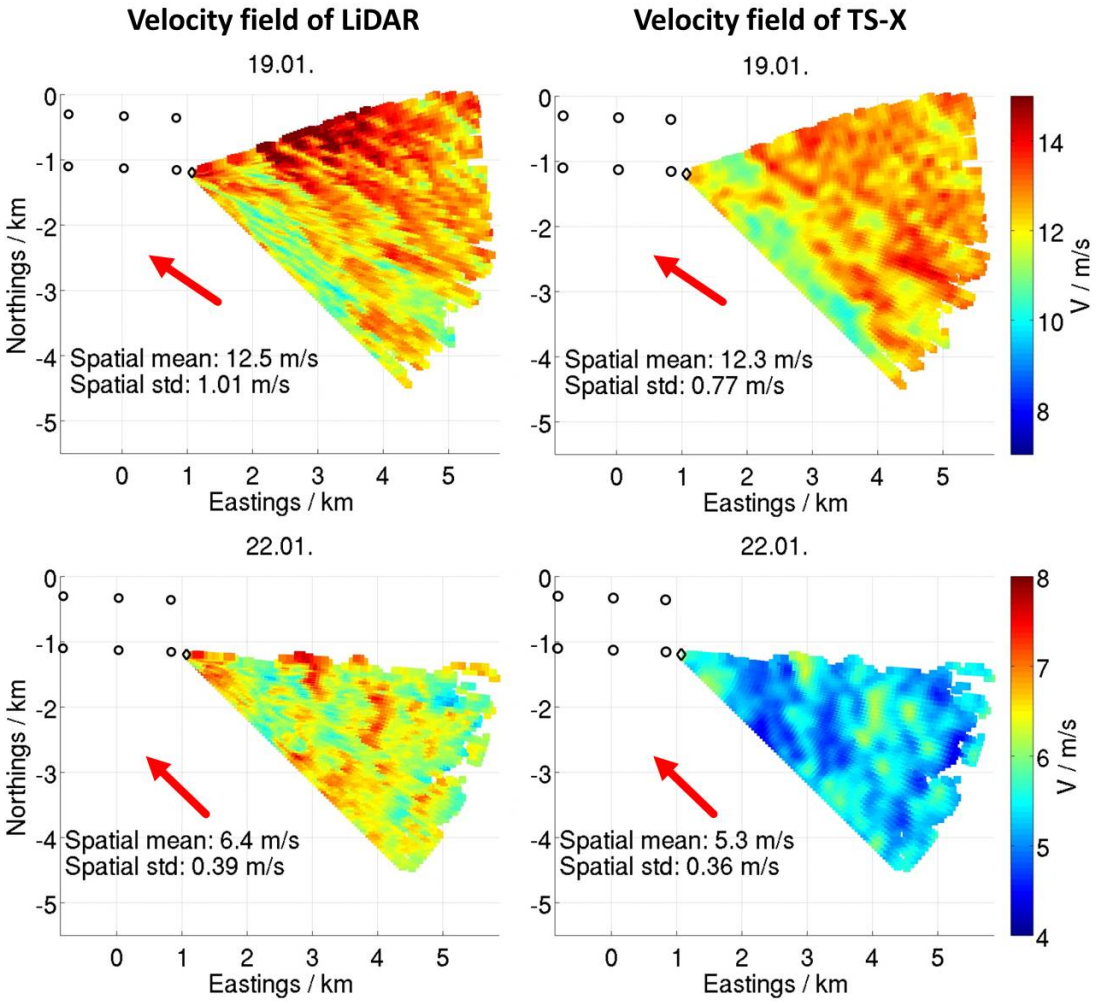

Figure 22: *Extrapolated wind field for LiDAR2 and TS-X wind field in* 10 *m height.*

tained with LiDAR2 since the data availability was highest for this system in free stream conditions (c.f. Appendix C). The calculated spatial averages and standard deviations of the remaining LiDAR systems and TS-X are listed in the Table 4. On the 19.01 high mean wind speeds up to 12.5 m/s occurred, while lowest mean wind speeds ranging from 5.3 m/s to 6.4 m/s are obtained on the 22.01. On the 17.01. a strong deviation in wind speed between LiDAR and TS-X data is observed. The spatial mean values of the different LiDAR and TS-X wind fields show good agreement for each measurement date with largest deviation of up to 0.7 m/s on the 16.01. Wind speed fluctuations expressed by the spatial standard deviation do have a general trend to increase with the wind speed, which can be explained by the increased wave height occurring at higher wind speeds resulting in

Table 4: Spatial average and standard deviation (in brackets) of processed LiDAR and TS-X wind fields. Note that three different sections from the TS-X wind field corresponding to the LiDAR system are used.

Measurement system	Unit	16.01.	17.01.	19.01.	22.01.
LiDAR1	m/s	8.6 (0.44)	10.4 (0.73)	11.3 (0.88)	-
LiDAR2	m/s	9.0 (0.49)	10.4 (0.69)	12.5 (1.00)	6.4 (0.39)
LiDAR3	m/s	9.2 (0.45)	10.9 (0.82)	12.4 (1.11)	6.7 (0.46)
TS-X1	m/s	7.7 (0.41)	6.4 (0.27)	12.0 (0.79)	-
TS-X2	m/s	8.4 (0.51)	6.1 (0.27)	12.3 (0.77)	5.3 (0.36)
TS-X3	m/s	7.8 (0.48)	6.4 (0.27)	12.1 (0.75)	5.6 (0.5)

stronger turbulent movement of the wind field (Türk and Emeis, 2007). A notable match of wind field structures can be seen on the 19.01. and 22.01., which is further quantified in Section 4.1.2.

In Figure 23 the time lag between the measurements of LiDAR2 and TS-X are illustrated. Note that due to the measurement principle of the LiDAR values on each radial beam are measured at the same time. In general a small time lag $|\Delta t| < 30\,\mathrm{s}$ with a continuous

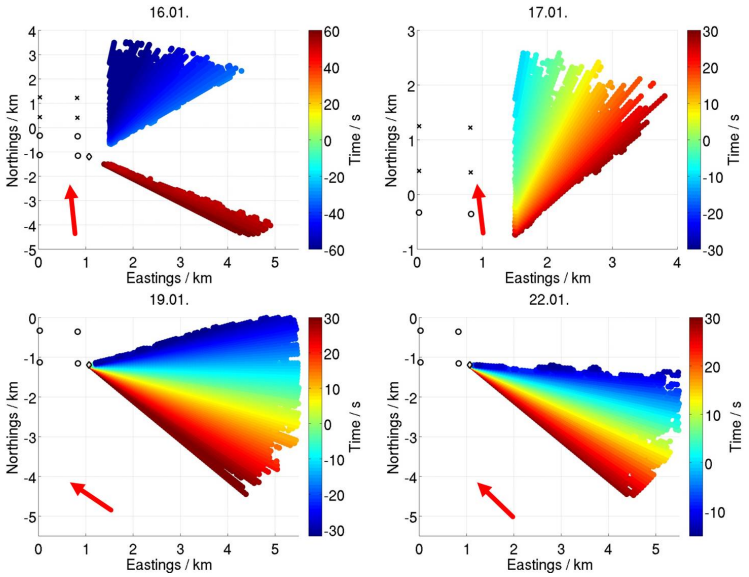

Figure 23: *Time lag between LiDAR2 and satellite measurement. The wind direction from COSMO-DE in* 10 *m height is indicated by a red arrow.*

distribution of measurement data is observed on the 17.01., 19.01. and 22.01. On the 16.01. a big time lag $|\Delta t| > 30\,\mathrm{s}$ is observed caused by the LiDAR measuring in excluded wind field sectors almost perpendicular to the wind flow during the TS-X measurement.

A wind field obtained from multi-LiDAR data is shown in Appendix D. Compared to measurements with a single LiDAR system the number of available data and covered area is significantly smaller, which is caused by a small intersection area of the conical PPI-Scan

trajectory. The amount of available measurements for multi-LiDAR data are shown in Appendix C. Due to the low amount of measurements a comparison of wind field structures is not carried out. In the table 5 the spatial average and standard deviation of the wind fields measured by multi-LiDAR and TS-X are shown. On the 17.01. no multi-LiDAR values were available in free stream conditions.

Table 5: Spatial average and standard deviation (in brackets) of processed multi-LiDAR and TS-X wind fields.

Measurement system	Unit	16.01.	17.01.	19.01.	22.01.
Multi-LiDAR	m/s	9.0 (0.32)	-	12.6 (0.57)	7.0 (0.54)
TS-X	m/s	8.4 (0.29)	-	12.2 (0.49)	5.3 (0.40)

4.1.1 Spatial averaged wind field difference

A first rough insight into the agreement of the wind fields on a large scale is provided by a spatial mean and spatial standard deviation of the difference between the wind fields from LiDAR and TS-X. In the following the used expressions mean and standard deviation refer to the spatial mean and spatial standard deviation in x and y direction of the wind field difference between LiDAR and TS-X. The mean and standard deviation of the difference between the wind fields of LiDAR2 and TS-X are plotted in Figure 24.

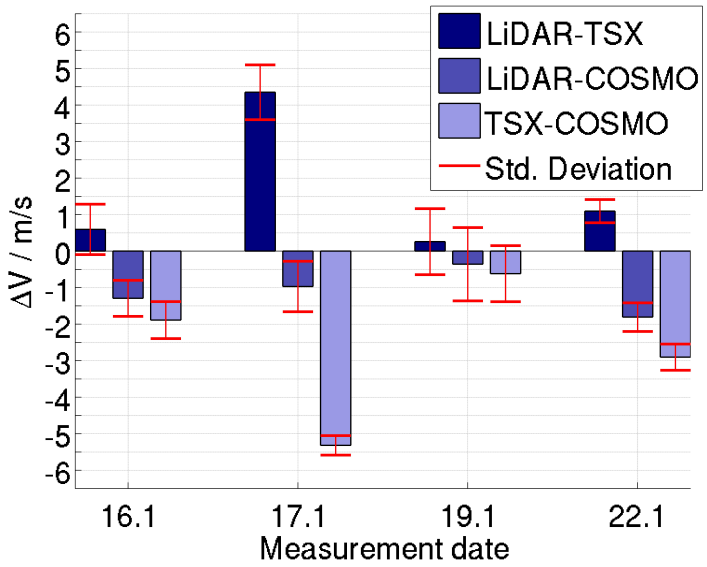

Figure 24: *Mean differences (bins) and standard deviations (red error bars) between LiDAR2, TS-X and COSMO-DE for the different measurement dates.*

On the 16.01 and 19.01. a very good agreement with mean differences smaller than 0.6 m/s and standard deviations of 0.69 m/s and 0.9 m/s were found. On the 22.01. a deviation of approximately 1.1 m/s with a standard deviation of 0.32 m/s is obtained still showing a good agreement. The results are in coincidence with the findings in (Schneiderhan, 2006), which show a mean difference of 0.6 m/s between measurements from the meterological

mast FINO1 and the SAR satellite ENVISAT. A very high deviation is observed on the 17.01. with a value of 4.3 m/s and a standard deviation of 0.75 m/s. Since the differences are positive on all dates the LiDAR measures higher wind speeds than TS-X. Similar results are also obtained for the remaining LiDAR systems shown in Appendix E with highest deviation of 0.8 m/s found on the 16.01. It has to be considered that the mean values are partly influenced by non-neutral stratifications of the atmosphere as a neutral profile was assumed for the height extrapolation of LiDAR data. This effect also applies for the neutral logarithmic profile used for the tuning dataset of the XMOD2 algorithm. As the atmospheric stability showed a trend to be unstable higher mean values have to be expected, particularly on the 22.01. (c.f. Section 3.4.2). However, the atmospheric stability will mainly influence the mean difference value while the standard deviation will remain almost unchanged.

A further error stems from the fluctuations of the vertical wind profile on small time scales, which are neglected in the height extrapolation method. A logarithmic shape of the profile is only ensured by averaging the turbulent fluctuations over a sufficiently large time interval of at least 10 min, which is longer than the interval times considered in this thesis. The deviation from the logarithmic profile is difficult to estimate and can only be described by a statistical approach. Recent research on this topic has been carried out in the work from (Behnken, 2014).

The differences between LiDAR2 and the wind speed values from the COSMO-DE model are −1.3 m/s on the 16.01., −1.0 m/s on the 17.01., −0.4 m/s on the 19.01. and −1.8 m/s on the 22.01 with COSMO-DE showing higher wind speed values than LiDAR2. Between TS-X and COSMO-DE data higher deviations are observed with mean wind speed differences of −1.9 m/s, −5.3 m/s, −0.7 m/s, −2.9 m/s on the 16.01., 17.01., 19.01. and 22.01., respectively.

In the case of the 17.01. a strong wind speed difference is observed between LiDAR and TS-X, which is likely to be caused by the TS-X data considering the high difference found in wind speed between COSMO-DE and TS-X. It was found that this high mismatch of TS-X is caused by an unusual low radar backscatter interpreted as low wind speeds by the XMOD2 algorithm. The reason for this low backscatter could be related to the high incidence angle of 49 ° used by TS-X on that day, which is outside the validation window of the XMOD2 algorithm. However, on the 19.01. the incidence angle was even slightly higher but shows normal radar backscatter and thus the low radar backscatter cannot be attributed to the high incidence angle alone. Also other meteorological phenomena altering the radar reflectivity of the ocean surface such as precipitation or boundary layer separation with independent wind flow layers can be excluded by archived weather information. An investigation carried out by the DLR of the radar backscatter map on the 17.01. revealed an uncommon situation. While the ambient mean wind speed is coming from a southerly sector the ocean waves are travelling almost perpendicular to the wind

direction in easterly direction. The reasons of the mismatch of the TS-X measurement are not fully understood and still under investigation. In the future the combined measurements of LiDAR and SAR could help to generate tuning datasets for further optimization of the XMOD2 algorithm.

Wind fields obtained from multi-LiDAR measurements have been compared with TS-X wind fields and are summarized in the Figure 25. Mean differences are obtained with values of 0.6 m/s, 0.5 m/s and 1.7 m/s on the 16.01., 19.01. and 22.01., showing slightly higher deviations than the results using single LiDAR data. Mean differences calculated from

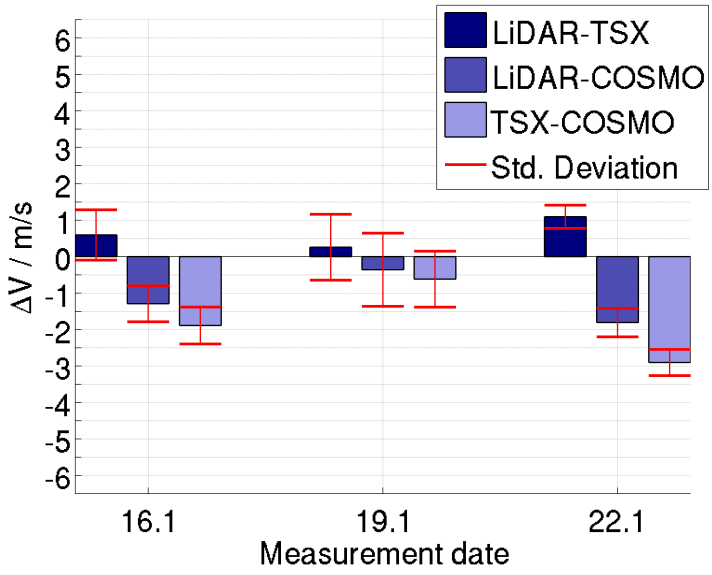

Figure 25: *Mean differences (bins) and standard deviations (red error bars) multi-LiDAR, TS-X and COSMO-DE for the different measurement dates.*

multi-LiDAR data compare surprisingly well with data from single LiDAR measurements although the amount of available measurements is much lower. However, the comparison of multi-LiDAR data by a spatial mean and standard deviation is questionable, since due to the low area coverage wind speeds values are not well Gaussian distributed. It can be assumed that the deviations between multi-LiDAR and single LiDAR measurements are mainly attributed to this effect. Nevertheless, multi-LiDAR has the potential to measure also in unfavourable wind speed sectors close to 90 ° and to have a higher measurement accuracy, since the wind direction error term $\Delta\vartheta$ from COSMO-DE does not apply (c.f. Section 3.4.1)

Finally it has to be noted that the agreement of wind fields can not be solely described by a mean and standard deviation, as wind fields with the same mean and standard deviation can exhibit a completely different arrangement of wind field structures. However, the comparison by a mean and standard deviation represents a robust method largely independent of the time lag between the measurement systems giving a first idea of the agreement of the wind fields.

4.1.2 Wind field structures

From the results shown in Figure 22 a good match of wind field structures can already be noticed especially on the 22.01. In order to better visualize the agreement of wind field structures the bias of 1.1 m/s in mean wind speed found on January 22 is added to the TS-X wind field in Figure 26.

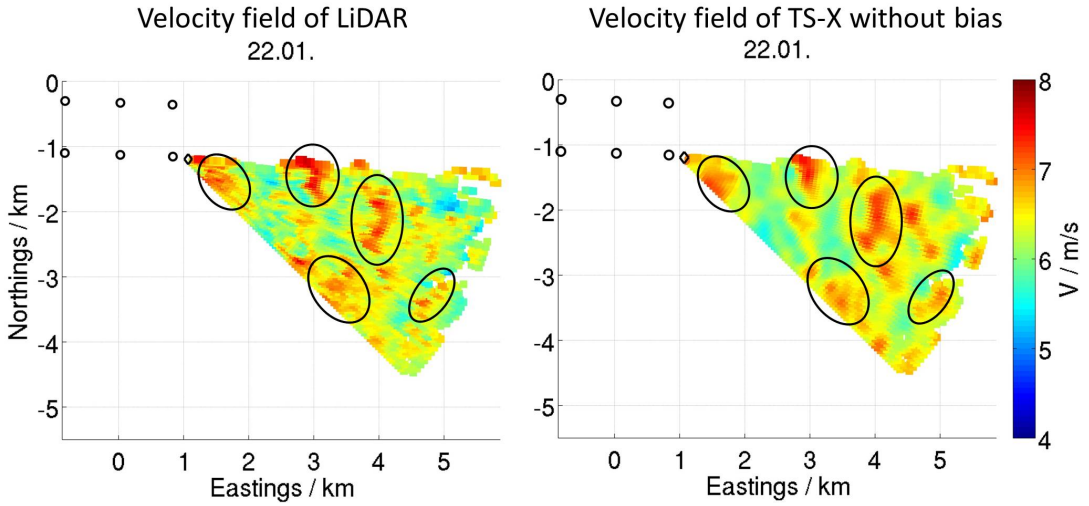

Figure 26: *Extrapolated wind field of LiDAR2 and TS-X wind field without bias in* 10 *m height above mean sea surface level.*

A very good agreement between the wind fields structures can be noticed which is indicated by black circles for some areas of the wind fields in the Figure 26. The good agreement is remarkable considering that TS-X derived the wind field from radar backscatter at the ocean surface, while LiDAR measured the wind field in far greater heights of up to 90 m above mean sea level which indicates that wind field structures are preserved even in greater height levels on this measurement day. While large and medium sized wind field structures seem do agree very well smaller wind field structures do not show a good match, which can be attributed to some extend to the time lag between LiDAR and satellite measurements. At this point it has to be considered at which spatial scales it makes sense to compare wind field structures by a linear correlation as the smaller dynamic scales of the wind field structures can not be well correlated except at a time lag of zero. In the future this could be investigated by application of a Box or Gaussian Filter on the wind field, which filters out smaller wind field structures.

In order to further quantify the agreement of wind field structures the linear correlation of values along each radial beam of the LiDAR and TS-X wind field are plotted over the time lag in Figure 27. The linear correlation coefficients tend to fluctuate strongly with each radial beam. In order to smooth these fluctuations and to make a trend visible a moving average with a 10 s sliding window is added. The comparison confirms the good agreement of wind field structures observed on the 22.01. with linear correlation coefficient reaching values of up to 0.75 around a time lag of zero and starts to reduce at higher time

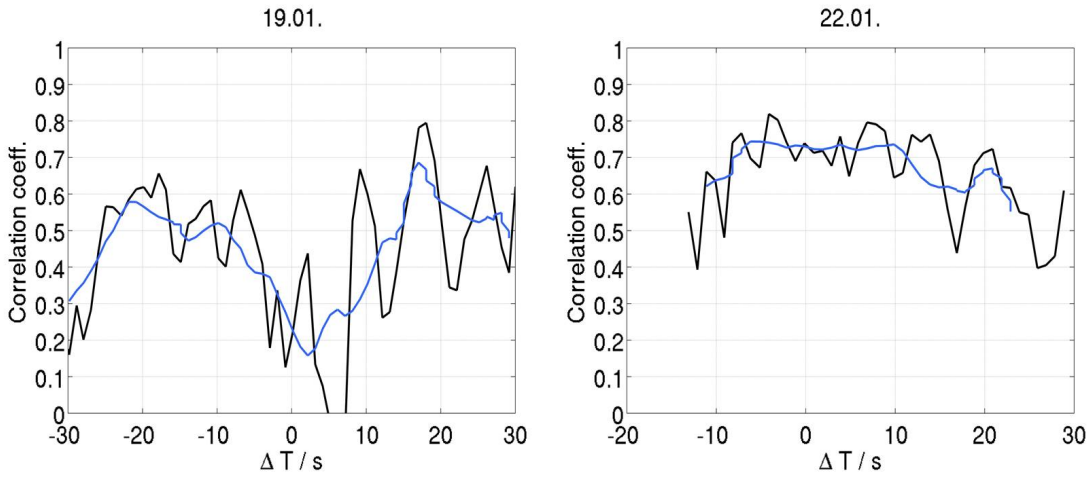

Figure 27: *Beamwise linear correlation coefficient in dependency of the time lag for the different measurement dates between LiDAR2 and TS-X. A 10 s sliding average (blue line) is added.*

lags of $|\Delta t| > 8\,s$. On the 19.01. strong fluctuations of the linear correlation are observed. The sliding average shows moderate linear correlations > 0.5 at time lags from $-25\,\mathrm{s}$ to $-10\,\mathrm{s}$ and $15\,\mathrm{s}$ to $30\,\mathrm{s}$. Also an unexpected strong reduction of the correlation coefficient around a time lag of zero occurs. A possible explanation for this low correlation are the high wind speeds of up to $15\,\mathrm{m/s}$ on this measurement date leading to higher turbulent intensities of the wind field and in consequence wind field structures are not likely to be contained in different height levels. Furthermore the amount of available tuning data for the XMOD2 algorithm was lower at these high wind speeds (Li and Lehner, 2014), which eventually leads to higher measurement errors by TS-X. No meaningful comparison of wind field structures were possible on the 16.01. and 17.01., due to a high time lag of $\Delta t > 30\,s$ between LiDAR and TS-X on the 16.01. and invalid data on the 17.01. observed by TS-X.

The remarkable match of wind field structures obtained on the 22.01. show the capability of TS-X to measure and reproduce structures of small scale wind field correctly from surface radar backscatter in free stream conditions and prove SAR derived wind fields to be a very promising method for future offshore wind field measurement. However, the influence of the meterological conditions on the agreement of wind field structures has to be further investigated.

4.2 Wake conditions

Wake patterns have been observed to different extend by TS-X and LiDAR on the measurement dates. The wake patterns observed in the wind fields from LiDAR and TS-X are shown in Appendix F. In the LiDAR data strong wake effects are observed on the 16.01., 17.01. and 22.01., while on the 19.01. the wake can hardly be distinguished from natural occurring low and high wind speed areas. Regarding the TS-X wind fields a wake development is clearly visible on the 22.01 and 16.01., respectively. On the 19.01 no wake patterns can be observed, which can be explained by the operation mode of the wind turbines in strong wind speeds. As the kinetic energy of the wind increases with the third exponent less velocity reduction of the wind flow is necessary to generate the same power output at higher wind speeds, which is usually achieved by pitching the rotor blades of the wind turbine. This greatly reduces the thrust coefficient of the wind turbine, resulting in smaller wake intensities according to current wake models (Tong et al., 2012). The weak wake pattern observed by TS-X on the 17.01. is presumably linked to the overall high mismatch of TS-X obtained on this date.

In this Section only data of LiDAR3 were considered for the comparison with TS-X, as it had the best conditions for wake measurements pointing almost directly into the wake with the smallest observed time lag of $\Delta t = 90 \pm 4\,s$. In the Figure 28 the wake tracks observed with LiDAR3 and TS-X are presented using a Cartesian grid with a resolution of 30 m in downstream direction and 13 m in lateral direction, which corresponds to the minimal spatial coverage of the LiDAR data at 17 D distance. It should be mentioned that the grid implies a finer resolution as can actually be provided by the measurement systems itself, but enables a sharper picture of the wake by creating additional data points at the grid points by linear interpolation. The height level of the wake measured by LiDAR3 is decreasing from 37.9 m in 6 D distance to 27.1 m in 17 D distance, while for TS-X the wake is measured at a fixed 10 m height level.

The wake is clearly visible in the LiDAR measurement with a wind speed reduction of approximately 60% at 4-5 rotor diameters downstream of the wind turbine located at 0 D. A significant recovery to almost 70% of the original wind speed can be observed, before the wake partly hits and merges with the wake of a second turbine at 10 D. In the TS-X data the wake is not sharply defined with a wind speed reduction of 25% in a wide region downstream of the wind turbine located at 0 D. This can be explained by the smaller strength of the wind turbine wake in lower height levels (c.f Section2.4). Similar values for the velocity deficit measured by TS-X where also obtained in the work of (Li and Lehner, 2014). Interestingly a maximum wake deficit with a wind speed reduction of up to 40% occurs at the regions of 8 D and 16 D, which can be interpreted as an effect of the wake expansion taking place behind the wind turbine with the wake fully influencing the ocean surface after a certain distance. However this effect is difficult to evaluate in the dataset here, since the wake is strongly influenced by the inflow and wake of neighboured turbines. Comparing the wake paths of LiDAR and TS-X, it can be seen that the wake tracks are

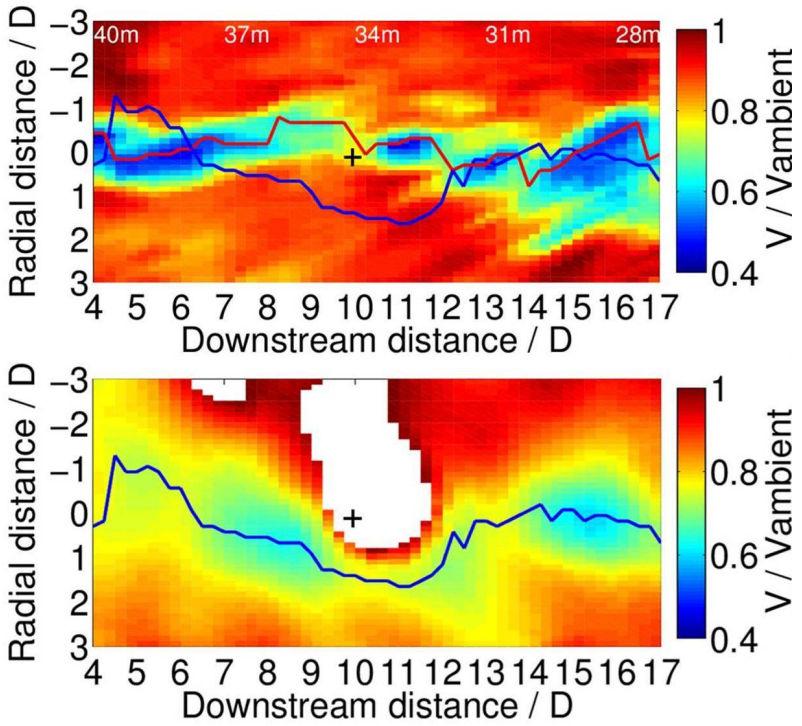

Figure 28: *Wake pattern observed by LiDAR3 (top) and TS-X (bottom) on January 22 downstream of wind turbine AV 12 located at* 0 *D. Wind speeds of LiDAR and TS-X are normalized by the spatial mean value of the LiDAR wind field at* 35 *m and the TS-X wind field at* 10 *m, respectively. The measurement heights of the LiDAR wind fields are displayed in white. The centre of the wake track is marked for the LiDAR measurement (red line) and the corresponding wake track from the TS-X measurement (blue line). The position of a second turbine is marked (+). Both axes are normalized with the rotor diameter* $D = 116\,m$ *of the wake generating turbine AV12. High wind speeds values caused by high radar backscatter on wind turbine structures are removed by hand.*

approximately in the same region but deviate from each other within 2 D lateral distance. This deviation is likely caused by wake meandering as a time lag between the wind fields was existent (Larsen et al., 2007). The LiDAR wake tracks shows stronger fluctuations especially at the region of 10 D to 14 D. This can be explained mainly by the interaction of the wakes from the turbines at 0 D and 10 D. Taking into account that wake is not necessarily a rotationally symmetric structure but also changes with the measurement height it seems reasonable that the LiDAR data shows more fluctuations in the wake track than TS-X as it measured in different height levels. The strong broadening of in the LiDAR wake at 15 D to 17 D can be also be attributed to the effects of wake merging.
Comparing the wake width, TS-X surprisingly observed a much broader wake than LiDAR in distances between 4 D to 10 D. Assuming an almost rotationally symmetric wake the wake should appear much narrower in lower height levels. A conceivable reason could be ocean current driven wakes behind the tower base, which superimposes the wind created wakes (Li et al., 2014). This effect should be further investigated in the future.

Considering the rather coarse resolution of 60 m, TS-X resolves maximal 3 points within one rotor diameter distance. This limits the maximum resolution possible within the wake.

However, TS-X can yield wind fields of higher spatial resolution, but with drawbacks in the wind speed accuracy. Despite these difficulties arising from differences in the location, the duration and time difference of the measurements and especially the fundamental differences in the measurement principle itself, the results obtained show the potential of TS-X to measure wake patterns behind wind turbines and should be further investigated in future measurement campaigns.

5 Conclusions and Outlook

The aim of this thesis is to investigate and evaluate the agreement between the wind fields from pulsed Doppler LiDAR and the SAR satellite TS-X in wake and free stream conditions.
For this purpose an algorithm is developed, which enables a comparison by processing the different spatial distributions of LiDAR and TS-X wind field data. In free stream conditions a height extrapolation of the LiDAR data down to the height level of TS-X is carried out assuming a neutral logarithmic vertical wind profile. The spatial agreement is compared by calculation of the difference between TS-X and LiDAR wind fields and a subsequent average in horizontal direction. Wind field structures are compared by a linear correlation between the values of LiDAR and TS-X data in dependency of the time lag. In wake conditions a height extrapolation by a logarithmic profile does not hold valid and wake tracks are compared at different height levels. The wake tracks are defined by the minimum of a Gaussian function fitted to the wake at various positions downstream of a wind turbine.

In free stream conditions the results revealed a good agreement between the LiDAR and TS-X wind fields. Spatial mean differences of 0.6 m/s, 0.3 m/s and 1.1 m/s and corresponding spatial standard deviations of 0.69 m/s, 0.9 m/s and 0.32 m/s were obtained on three of the four available measurement days. The results are within the measurement accuracy of TS-X (1.46 m/s) (Li and Lehner, 2014) confirming that SAR is able to retrieve the wind field on a coarse horizontal resolution. On the remaining date a very high deviation of almost 4.5 m/s occurred due to unusual low radar backscatter values observed by TS-X. The reasons for this low backscatter are presumably caused by a special meterological situation with ocean waves travelling almost perpendicular to the ambient wind direction. Regarding wind field structures a very good match was obtained on one of the four measurement dates with a linear correlation coefficient > 0.7 for small time lags between LiDAR and TS-X. This result is remarkable considering the different measurement principles and height levels of LiDAR and SAR, which shows that in free stream conditions wind field structures can indeed be correctly retrieved from SAR derived wind fields. Nevertheless, the influence of meteorological conditions on the results need to be further investigated.
The wake tracks obtained with LiDAR and TS-X are located in the same region downstream of the wind turbine but are not correlated. As a time lag of $[90 \pm 4]\,s$ between both measurements was existent this deviation is likely to be caused by wake meandering. Further deviations stem from the different shape of the wake at different height levels and the coarse horizontal resolutions of TS-X wind field data, which can not fully resolve the wake. In wake conditions a good agreement could neither be confirmed nor disproved and should be further investigated in the future using contemporary measurements between LiDAR and TS-X.

Uncertainties in the comparison method arise from non-neutral stratifications of the atmosphere assumed for the height extrapolation method. COSMO-DE data indicated a trend to unstable conditions during the measurement dates. Therefore a correction of the atmospheric stability should be applied, but this information is not always available. However, a change of the stability parameter will mainly affect the spatial mean difference, while the arrangement of wind field structures is almost unaffected.

A future research possibility is to investigate the dependency between the linear correlation coefficient and the size of wind field structures. This can be carried out in example by application of a Box or Gaussian filter removing small scale wind field structures, which would possibly lead to an overall higher linear correlation.
Another interesting idea is to reshape the LiDAR wind field to resemble the LiDAR wind field at the measurement time of the TS-X satellite. Assuming Taylor's hypothesis (Taylor, 1938) this could be carried out by shifting single LiDAR data along the wind direction in accordance to the time lag. However, the success of this method depends strongly on the scale of the wind field structures, as smaller wind field structures possibly do not meet Taylor's hypothesis (Higgins et al., 2012).
In future measurement campaigns combined usage of SAR satellite and LiDAR can help to better tune the SAR wind field retrieval algorithms. Based on the findings of this thesis, recommendations for the LiDAR measurement set-up in future campaigns can be proposed. For a better knowledge about the prevailing wind profile the LiDAR should measure the vertical wind profile before the satellite measurements take place. During the satellite measurements the LiDAR switches into a flat PPI scan mode. To reduce the uncertainty of the height extrapolation the measurement height of the PPI scan should be as close as possible to the height level of TS-X measurements. As the LiDAR typically is positioned higher than the measurement height of TS-X this can be achieved by scanning with a small negative elevation angle, which could also deliver information about the prevailing vertical profile in that height level. To reduce the time lag between LiDAR and TS-X measurements the LiDAR scan trajectory can be optimized by measuring in a small sector with azimuth angles of $\pm 40\,^{\circ}$ from the ambient wind direction. For measurements in wake conditions a higher spatial wind field resolutions should be used both by LiDAR and TS-X in order to better resolve the wake structure.
In the future the availability of satellite imagery will strongly increase. A step in this direction are the launch of the SAR satellite *Sentinel-1A* in 2014 followed by *Sentinel 1-B* planned for 2016. This enables an extensive generation of tuning datasets from combined LiDAR and SAR satellite measurements with the final goal to use SAR satellite independent from LiDAR for the retrieval of small scale offshore wind fields.

References

Aitken, M., Banta, R., Pichugina, Y. and Lundquist, J.; Quantifying Wind Turbine Wake Characteristics from Scanning Remote Sensor Data; *Journal of Atmospheric and Oceanic Technology*; volume 31, 765 – 787; doi:10.1175/JTECH-D-13-00104.1; 2014.

Badger, M., Diaz, A., Bredesen, R., Berge, E., Hahmann, A. and Badger, J.; Bringing satellite winds to hub-height; in *Proceedings of EWEA 2012 - European Wind Energy Conference & Exhibition*; 2012.

Baldauf, M., Förstner, J., Klink, S., Reinhardt, T., Schraff, C., Seifert, A. and Stephan, K.; Kurze Beschreibung des Lokal-modells Kürzestfrist COSMO-DE (LMK) und seiner Datenbanken auf dem Datenserver des DWD; Technical report; Deutscher Wetterdienst (DWD) Geschäftsbereich Forschung und Entwicklung, Offenbach; 2009.

Barthelmie, R., Pryor, S., Frandsen, S., Hansen, K., Schepers, J., Rados, K., Schlez, W., Neubert, A., Jensen, L. and Neckelmann, S.; Quantifying the Impact of Wind Turbine Wakes on Power Output at Offshore Wind Farms; *J. Atmos. Oceanic Technol.*; volume 27, 8, 13021317; doi:10.1175/2010jtecha1398.1; 2010.

Beck, H., Trujillo, J and Kühn, M.; Analysis of wake sweeping effects based on load and long-range lidar measurements; in *Proceedings of DEWEK*; 2015.

Behnken, C.; Stochastische Charakterisierung des Offshore Windprofiles auf kurzen Zeitskalen; Master's thesis; Carl von Ossietzky Universität Oldenburg; 2014.

Burton, T., Jenkins, N., Sharpe, D. and Bossanyi, E.; *Wind Energy Handbook*; John Wiley & Sons, Ltd; ISBN 9780470699751; doi:10.1002/9781119992714; 2011.

Butler, J., Quail, F., Torr, R. and More, G.; Comparison of scanning lidar offshore wake measurements with industry standard and complex models; in *Proceedings of EWEA Offshore*; 2013.

Cañadillas, B., Westerhellweg, A. and Neumann, T.; Testing the Performance of a Ground-based Wind LiDAR System. One Year Intercomparison at the Offshore Platform FINO1; *DEWI Magazin*; volume 38, 58–64; URL `http://www.dewi.de/dewi/fileadmin/pdf/publications/Magazin_38/08.pdf`; 2011.

Cariou, J. and Boquet, M.; Leosphere Pulsed Lidar Principles - Contribution to UpWind WP6 on Remote Sensing Devices; Technical report; Leosphere; 2010.

Corbetta, G., Mbistrova, A., Ho, A., Guillet, J., Pineda, I. and Wilkes, J.; The European offshore wind industry- key trends and statistics 2014; Technical report; European Wind Energy Association (EWEA); 2015.

Emeis, S.; *Wind Energy Meteorology*; Springer Berlin Heidelberg; ISBN 978-3-642-30523-8; doi:10.1007/978-3-642-30523-8; 2013.

Fritz, T. and Eineder, M.; TerraSAR-X Ground Segment - Basic Product Specification Document; Technical report; DLR; 2008.

Gottschall, J., Wolken-Möhlmann, G., Viergutz, T. and Lange, B.; Results and Conclusions of a Floating-lidar Offshore Test; *Energy Procedia*; volume 53, 156161; doi: 10.1016/j.egypro.2014.07.224; 2014.

Hasager, C., Vincent, P., Badger, J., Badger, M., Bella, A., Pena, A., Husson, R. and Volker, P.; Using Satellite SAR to Characterize the Wind Flow around Offshore Wind Farms; *Energies, 8, 5413-5439*; doi:10.3390/en8065413; 2015.

Hersbach, H.; CMOD5.N: A C-band geophysical model function for equivalent neutral wind; Technical report; European Centre for Medium-Range Weather Forecasts; 2008.

Higgins, C., Froidevaux, M., Simeonov, V., Vercauteren, N., Barry, C. and Parlange, M.; The Effect of Scale on the Applicability of Taylor's Frozen Turbulence Hypothesis in the Atmospheric Boundary Layer; *Boundary-Layer Meteorol*; volume 143, 2; doi: 10.1007/s10546-012-9701-1; 2012.

Holt, B.; SAR Imaging of Ocean Surface; in C. Jackson and J. Apel, editors, *Synthetic Aperture Radar (SAR) Marine Users Manual*; chapter 2, pp. 25–79; NOAA NESDIS Office of Research and Applications; URL `http://www.sarusersmanual.com/ManualPDF/NOAASARManual_CH02_pg025-080.pdf`; 2004.

Iungo, G. V. and Porté-Agel, F.; Volumetric scans of wind turbine wakes performed with three simultaneous wind LiDARs under different atmospheric stability regimes; *Journal of Physics: Conference Series*; volume 524; doi:10.1088/1742-6596/524/1/012164; 2014.

Jackson, C. and Apel, J.; *Synthetic Aperture Radar (SAR) Marine Users Manual*; NOAA NESDIS Office of Research and Applications; URL `http://www.sarusersmanual.com/ManualPDF/NOAASARManual_FrontMatter.pdf`; 2004.

Käsler, Y., Rahm, S., Simmet, R. and Kühn, M.; Wake Measurements of a Multi-MW Wind Turbine with Coherent Long-Range Pulsed Doppler Wind Lidar; *Journal of Atmospheric and Oceanic Technology*; volume 27, 9, 1529–1532; doi:10.1175/2010JTECHA1483.1; 2010.

Kindler, D. and Oldroyd, A.; NORSEWInD: First Offshore LiDAR Deployments; in *Poster Presentation EWEC 2010, Warsaw, Poland*; 2010.

Lange, M.; Analysis of the Uncertainty of Wind Power Predictions; Ph.D. thesis; Carl von Ossietzky Universität Oldenburg; 2003.

Larsen, G., Madsen, H., Bingöl, F., Ott, S., Sørensen, J., Okulov, V., Troldborg, N., Nielsen, M., Thomsen, K., Larsen, T. and Mikkelsen, R.; Dynamic wake meandering modeling; Technical report; RISØ; 2007.

Lee, S., Churchfield, M., Moritarty, P., Jonkman, J. and Michalakes, J.; Atmospheric and Wake Turbulence Impact on Wind Turbine Fatigue Loading; in *50th AIAA Aerospace Sciences Meeting*; National Renewable Energy Laboratory (NREL); 2012.

Leosphere; *User Manual Windcube100S/200S*; Leosphere; Orsay, France; 2012.

Li, X., Chi, L., Chen, X., Ren, Y. and Lehner, S.; SAR observation and numerical modeling of tidal current wakes at the East China Sea offshore wind farm; *J. Geophys. Res. Oceans*; volume 119, 8; doi:10.1002/2014jc009822; 2014.

Li, X. and Lehner, S.; Observation of TerraSAR-X for studies on offshore wind turbine wake in near and far fields; *IEEE Journal of selected topics in Applied Earth Observations and Remote Sensing*; volume 6, 3; doi:10.1109/JSTARS.2013.2263577; 2013.

Li, X. and Lehner, S.; Algorithm for Sea Surface Wind Retrieval From TerraSAR-X and TanDEM-X Data; *IEEE Transactions on Geoscience and Remote Sensing*; volume 52, 5; doi:10.1109/tgrs.2013.2267780; 2014.

McCandless, S. and Jackson, C.; Principles of Synthetic Aperture Radar; in C. Jackson and J. Apel, editors, *Synthetic Aperture Radar (SAR) Marine Users Manual*; chapter 1, pp. 1–25; NOAA NESDIS Office of Research and Applications; URL `http://www.sarusersmanual.com/ManualPDF/NOAASARManual_CH01_pg001-024.pdf`; 2004.

Moiera, A.; Synthetic Aperture Radar (SAR): Basics, Theory and Future Developments; German Aerospace Center (DLR); 2014.

Neumann, T., Nolopp, K., Riedel, V., Strack, M., Herklotz, K. and Stein, J.; Assessment of One Year Wind Measurements on the First Offshore Wind Research Platform in the German Bight - FINO1; in *Proceedings of DEWEK 2004*; 2004.

Obukhov, A.; Turbulence in an atmosphere with a non-uniform temperature; *Boundary-Layer Meteorology*; volume 2, 1; doi:10.1007/bf00718085; 1971.

Queffeulou, P.; Accuracy of Wind Measurements Performed on Buoys, Ship, and Island during the TOSCANE-2 Experiment; *J. Atmos. Oceanic Technol.*; volume 8, 6; doi:10.1175/1520-0426(1991)008⟨0835:aowmpo⟩2.0.co;2; 1991.

Ren, Y., Lehner, S., Brusch, S., Li, X. and He, M.; An algorithm for the retrieval of sea surface wind fields using X-band TerraSAR-X data; *International Journal of Remote Sensing*; volume 33, 23; doi:10.1080/01431161.2012.685977; 2012.

Sanderse, B.; Aerodynamics of wind turbine wakes; Technical report; ECN Energy research Centre of the Netherlands; 2009.

Satheesan, K., Sarkar, A., Parekh, A., Ramesh Kumar, M. and Kuroda, Y.; Comparison of wind data from QuikSCAT and buoys in the Indian Ocean; *International Journal of Remote Sensing*; 2015.

Schneemann, J., Bastine, D., van Dooren, M., Schmidt, J., Steinfeld, G., Trabucchi, D, Trujillo, J., Vollmer, L and Kühn, M.; "GW Wakes": Measurements of wake effects in alpha ventus with synchronized long range LIDAR windsanners; in *DEWEK*; 2015.

Schneemann, J., Trabucchi, D., Trujillo, J. and Kühn, M.; Comparing measurements of the horizontal wind speed of a 2D Multi-Lidar and a cup anemometer; *Journal of Physics: Conference Series*; volume 555, 012091; doi:10.1088/1742-6596/555/1/012091; 2014.

Schneiderhan, T.; Nutzung satellitengestützter SAR-Daten und des CMOD4-Modells zur Untersuchung des lokalen Windfeldes in der Umgebung von Offshore-Windparks; Ph.D. thesis; Ludwig-Maximilians-Universität München (LMU); 2006.

Stawiarski, C., Träumner, K., Knigge, C. and Calhoun, R.; Scopes and Challenges of Dual-Doppler Lidar Wind Measurements An Error Analysis; *J. Atmos. Oceanic Technol.*; volume 30, 9; doi:10.1175/jtech-d-12-00244.1; 2013.

Taylor, G.; The Spectrum of Turbulence; in *Proceedings of the Royal Society of London. Series A, Mathematical and Physical Sciences*; volume 164; pp. 476–490; 1938.

Tong, W., Chowdhury, S., Zhang, J. and Messac, A.; Impact of Different Wake Models On the Estimation of Wind Farm Power Generation; *12th AIAA Aviation Technology, Integration, and Operations (ATIO) Conference and 14th AIAA/ISSMO Multidisciplinary Analysis and Optimization Conference*; doi:10.2514/6.2012-5430; 2012.

Trabucchi, D.; Script Wind Physics Measurement Project, Sommersemester 2013; ForWind University of Oldenburg; 2013.

Türk, M. and Emeis, S.; Abhängigkeit der Turbulenzintensität über See von der Windgeschwindigkeit; in *DEWI Magazin Nr. 30*; DEWI; 2007.

van Dooren, M.; Analysis of Multiple-Doppler LIDAR Data for the Characterization of Wakes in an OffshoreWind Farm; Master's thesis; Carl von Ossietzky Universität Oldenburg, Technical Universtiy of Denmark (DTU); 2014.

Vollmer, L., van Dooren, M., Trabucchi, D., Schneemann, J., Steinfeld, G., Witha, B., Trujillo, J. and Kühn, M.; First comparison of LES of an offshore wind turbine wake with dual-Doppler lidar measurements in a German offshore wind farm; *Journal of Physics: Conference Series*; volume 625, 1, 012001; URL `http://stacks.iop.org/1742-6596/625/i=1/a=012001`; 2015.

Weitkamp, C., Wandinger, U., Werner, C., Sassen, K., Bissonnette, L., Ansmann, A., Müller, D., Eloranta, E., Streicher, J., Leike, I., Münkel, C., Gimmestad, G., Bösenberg, J., Behrent, A., Abo, M., McCormick, M., Theopold, F., Wolf, J. and Wöste, L.; *Lidar Range-Resolved Optical Remote Sensing of the Atmosphere*; Springer-Verlag; ISBN 978-0-387-40075-4; doi:10.1007/b106786; 2005.

Werner, Christian; Doppler Wind Lidar; in Claus Weitkamp, editor, *Lidar*; volume 102 of *Springer Series in Optical Sciences*; chapter 12, pp. 325–354; Springer Berlin / Heidelberg; ISBN 978-0-387-40075-4; doi:10.1007/0-387-25101-4_12; 2005.

Werner, C., Stephan, R., Lehner, S. and Buchhold.M.; Comparison of ERS-2 SAR wind measurements with an airborne Doppler lidar wind measurement; in *Proc. SPIE 3218, Laser Radar Ranging and Atmospheric Lidar Techniques, 154*; doi:10.1117/12.295652; 1997.

Werner, C., Streicher, J., Reitenbuch, O., Nagel, E., Schneiderhan, T., König, T., Lehner, S., Banakh, V., Falits, A., Dabas, A. and Delville, P.; Wind and turbulence measurements over sea by Doppler lidar and SAR; *Atmos. Oceanic Opt.*; volume 17, 8; 2004.

Appendices

A

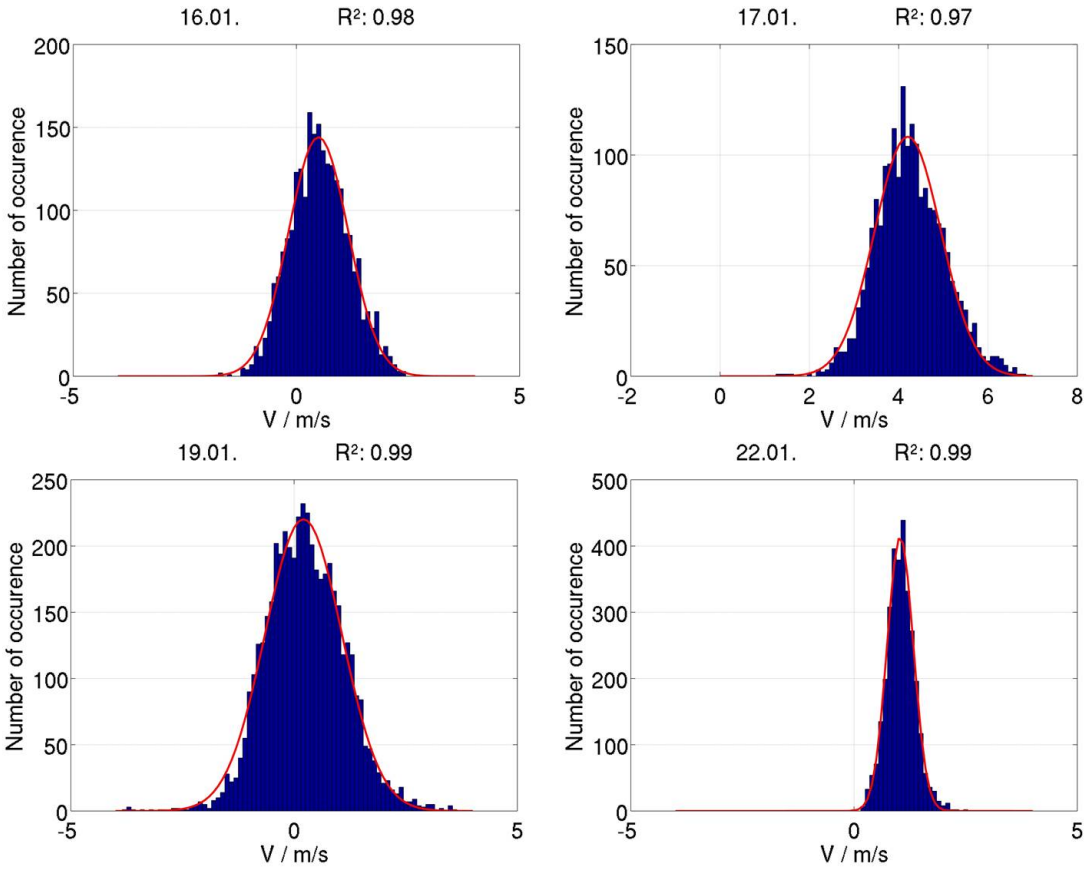

Figure 29: *Histogram plot of processed wind field difference with a bar width of* 0.1 *m/s. A Gaussian fit is added by a least squared method (red curve). The fit quality parameter* R^2 *is shown in the title.*

B

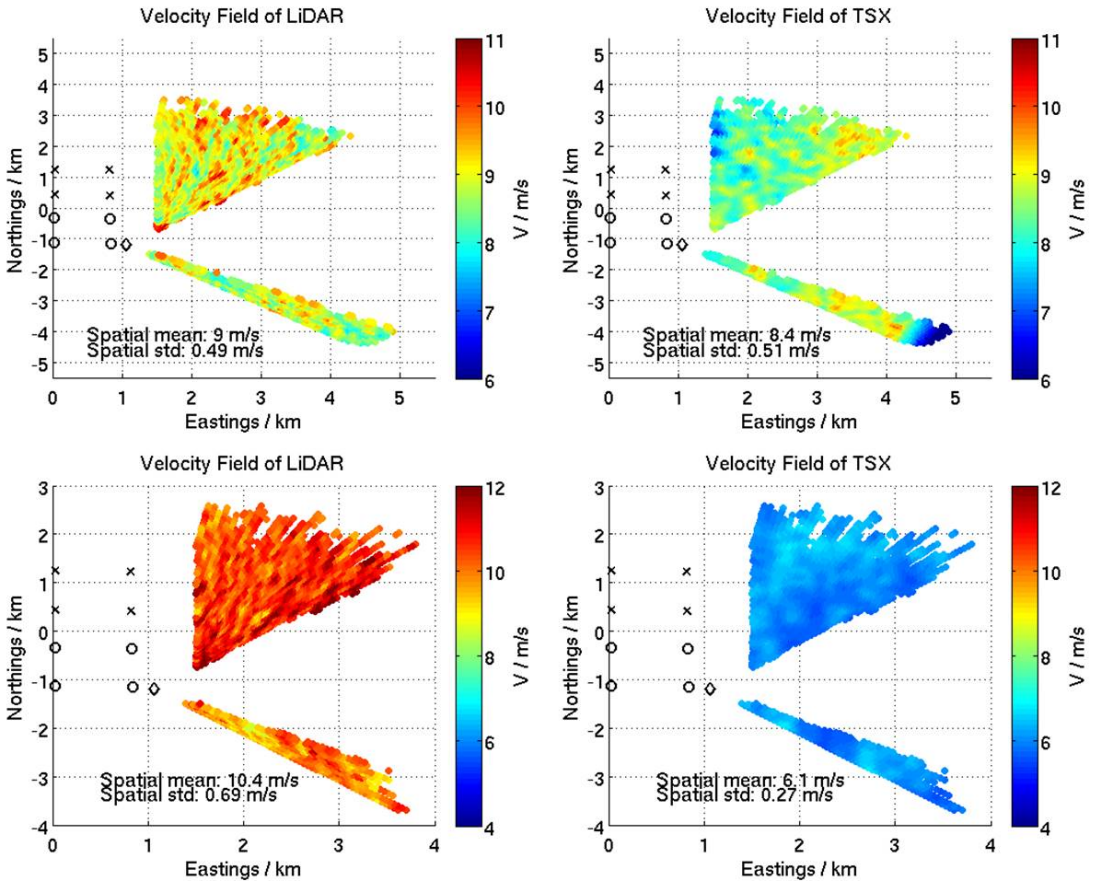

Figure 30: *Extrapolated wind field for LiDAR2 and TS-X wind field in 10 m height obtained on the (top row) 16.01. and (bottom row) 17.01.*

C

Table 6: Amount of available measurement data from LiDAR systems.

Measurement system	16.01.	17.01.	19.01.	22.01.
LiDAR1	1541	475	1554	-
LiDAR2	2481	1968	4805	3105
LiDAR3	2107	484	2685	2241
Multi	107	-	278	246

D

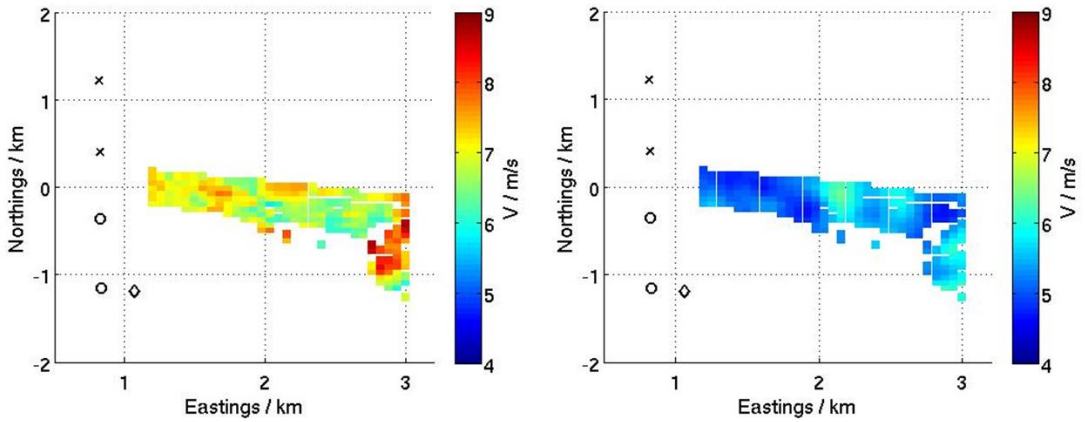

Figure 31: *Extrapolated wind field from multi-LiDAR measurements (left) and TS-X (right) in* 10 *m height measured on January 22.*

E

Table 7: Spatial mean differences and spatial standard deviations (in brackets) between wind fields of all available LiDAR systems and TS-X, all available LiDAR systems and COSMO and between TS-X and COSMO. Note that three different sections from the TS-X wind field corresponding to the LiDAR system are used.

Measurement system	Unit	16.01.	17.01.	19.01.	22.01.
LiDAR1 - TSX	m/s	0.9 (0.62)	4.0 (0.69)	-0.7 (1.08)	-
LiDAR2 - TSX	m/s	0.6 (0.69)	4.3 (0.75)	0.3 (0.9)	1.1 (0.32)
LiDAR3 - TSX	m/s	1.4 (0.65)	4.6 (0.78)	0.4 (1.26)	1.2 (0.58)
Multi - TSX	m/s	0.6 (0.42)	-	0.5 (0.67)	1.7 (0.65)
LiDAR1 - COSMO	m/s	-1.8 (0.44)	-1.1 (0.73)	-1.5 (0.88)	-
LiDAR2 - COSMO	m/s	-1.3 (0.49)	-1.0 (0.69)	-0.4 (1.00)	-1.8 (0.40)
LiDAR3 - COSMO	m/s	-1.2 (0.45)	-0.5 (0.82)	-0.4 (1.11)	-1.5 (0.46)
Multi - COSMO	m/s	-1.3 (0.32)	-	-0.2 (0.57)	-1.2 (0.54)
TSX1 - COSMO	m/s	-2.6 (0.41)	-5.0 (0.27)	-0.8 (0.79)	-
TSX2 - COSMO	m/s	-1.9 (0.51)	-5.3 (0.27)	-0.6 (0.77)	-2.9 (0.36)
TSX3 - COSMO	m/s	-2.5 (0.48)	-5.0 (0.27)	-0.8 (0.75)	-2.6 (0.50)
TSXMulti - COSMO	m/s	-1.9 (0.29)	-	-0.71 (0.49)	-2.9 (0.40)

F

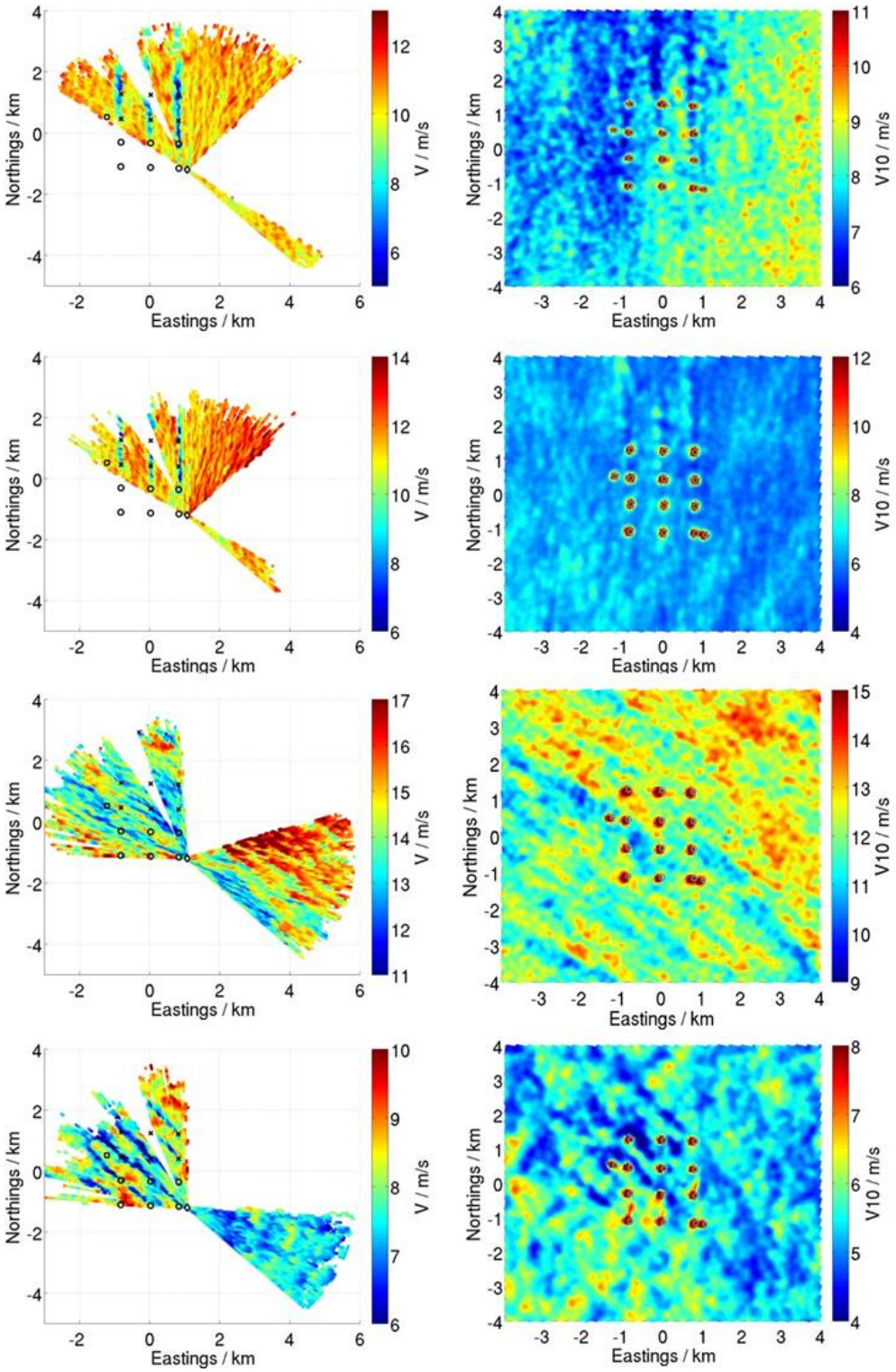

Figure 32: *Wind fields measured by LiDAR2 (left) and TS-X wind field (right) in 10 m height for the dates 16.01.(top row), 17.01.(second row), 19.01.(third row), 22.01.(bottom row). Wake development is visible behind the wind turbines.*